

# **Zinc Sulfide-Based Hybrid Exosome-Coated Autophagy-Mediated H<sub>2</sub>S-sensitized PDT/chemotherapeutic Synergistic Nanoplatfrom for Targeted Treatment of Glioblastoma Stem-Like Cells in Orthotopic Mouse Glioblastoma Model**

Jingxin Mo<sup>\*1,2</sup>, Meiying Li<sup>1,3</sup>

<sup>1</sup> *Clinical Research Center for Neurological Diseases of Guangxi Province, The Affiliated Hospital of Guilin Medical University, Guilin 541001, China,*

<sup>2</sup> *School of Chemistry, University of New South Wales, Sydney, New South Wales 2052, Australia,*

<sup>3</sup>*School of Pharmacy, Guilin Medical University, Guilin 541001, China.*

Correspondent E-mail:

Jingxin Mo: [Jingxin.mo@hotmail.com](mailto:Jingxin.mo@hotmail.com)

## Abstract

To eliminate glioblastoma stem-like cells, fine core-shell nanoparticles, consisting of hollow ZnS nanoparticles covered by hybrid exosome shell containing exosome and dual responsive iRGD derived phosphatidylserine, and incorporated with autophagic inhibitor hydroxychloroquine (HCQ), denoted as HCQ@ZnS@exo@iRGD were synthesized, characterized and evaluated *in vitro* and *in vivo*. The highest release performance of HCQ from HCQ@ZnS@exo@iRGD was attained under low pH and high glutathione conditions. Hybrid exosomes enabled the glioblastoma stem-like cells (GSCs) targeting properties along with excellent permeated ability across BBB were observed both in 3D cells spheroids and in orthotopic mouse glioblastoma model. Visible light source is used to trigger the ROS induction of hollow ZnS nanopartilces. Meanwhile ZnS could produce H<sub>2</sub>S gas and release its cargo of HCQ as well *in situ*. Consequently, significant targeted damage to GSCs is achieved due to the combined cytotoxic effects and autophagy-deactivation enabled by HCQ@ZnS@exo@iRGD nanocomposites, indicating its considerable potential for effective GBM treatment.

**Keywords:** Glioblastoma stem-like cells; Zinc sulfide; Autophagy flux; Internalizing RGD peptide; Photodynamic therapy; Exosome.

## 1. Introduction

Glioblastoma (GBM) is the most common malignant brain tumor in adults and remains incurable despite surgery, radiation, and chemotherapy. The median survival of patients with GBM is just over 1 year.[1] This poor outcome is due in part to the so-called glioblastoma stem or stem-like cells (GSCs). With diverse differentiation potential and unique properties of invasiveness, proliferation, self-renewing and resistance to therapy, these GSCs are considered responsible for tumor recurrence.[2] Furthermore, Genome sequencing and transcriptional profiling studies have highlighted a large number of genetic events and identified multiple biologically relevant GBM subtypes, representing a major challenge for targeted therapy.[3]

Photodynamic therapy (PDT) is driven by the induction of reactive oxygen species (ROS) from a photosensitizer under light irradiation to damage cellular organelles.[4] The efficacy of PDT in treating tumor suffers daunting challenges due to the elevated autophagy's activities allows tumor cells to survive under metabolic and therapeutic stress such as ROS.[5] Thus, autophagy inhibition has emerged as a promising target for combination drug therapies. The lysosomotropic agent hydroxychloroquine (HCQ) can inhibit autophagy to some extent and has been used in several preclinical and clinical trials for sensitizing tumors to chemotherapy.[6] However, a major challenge with HCQ is the drug shows nonselective distribution *in vivo*. [7] In addition, the high metabolic rate of tumors often leads to an acidic tumor microenvironment (TME) with higher glutathione (GSH) concentration, which caused drug hydrolyzed and inactivated.[8] More importantly, due to the blood-brain barrier (BBB) and the elusive location of GSCs. It's even harder for HCQ, which is highly hydrophilic, to pass BBB and get to GSCs for exerting its pharmacological effect.[9] Thus, methods are urgently needed to deliver HCQ selectively to tumors, overcome the barriers of BBB and TME and improve HCQ concentration within GSCs.

Zinc sulfide (ZnS) is an atypical transition-metal sulfid with various morphologies, such as quantum dots (QDs), nanorods/nanowires, nanobelts, nanotubes, nano-ribbon array, nanoporous particles and hollow spheres.[10] The hollow ZnS has received intensive attention recently based on the merits of hollow micro/nano structures. The hollow ZnS nanoparticles have a high surface-to-volume ratio and surface states are useful for drug delivery in terms of drug loading capacity and surface modification.[11] More recently, ZnS has received special attention the field of photodynamic therapy (PDT) due to its strong light-response activity originated from their large energy gap (~3.7 eV). Since the energy of photons from hollow ZnS nanoparticles is equal or higher than the bandgap, energy (electrons) transfer takes place from the valence band (VB) to the conduction band (CB), which is due to the formation of a hole (VB) and electron (CB). VB ( $h^+$ ) reacts with  $H_2O$  and generates  $OH^\bullet$  radical. CB ( $e^-$ ) reacts with oxygen, and initiate the reduction process and produces  $OH^\bullet$  radical.[12] More importantly, in acidic microenvironment of tumor and especially lysosome, ZnS would produce hydrogen sulfide ( $H_2S$ ). [13]  $H_2S$ , similar to carbon monoxide (CO) and nitric oxide (NO) as an endogenous gaseous transmitter, is known to play a crucial role in physiological and pathophysiological processes. The presence of high concentration of  $H_2S$  induces selective inhibition of tumor cells due to the distinctive sulfhydrylation of

protein of tumor cells.[14]

The 3-amino-acid sequence ArgGlyAsp (RGD) is a tissue-specific peptide. The original toroidal RGD peptide, denoted as internalized RGD (iRGD), shows satisfactory histiocyte penetration and tumor targeting.[15] The iRGD peptide interacts with overexpressed  $\alpha\beta3$  or  $\alpha\beta5$  integrins in neoplastic vasculature and binds to the neuropilin-1 receptor of cancer cells, which would further induce cellular internalization, vascular leakage, and penetration into extravascular tumor tissue.[16] Thus, functionalizing ZnS nanoparticles with iRGD as targeted ligand may improve BBB crossing to specifically accumulate in tumor site for the advanced glioma therapy. Exosomes are 30-120 nm microvesicles secreted by variety of cells through exocytosis that can exert a wide variety of biological effects on target cells.[17] The exosome consists of a bilipid layer containing embedded proteins and RNA, which are stabilized by its three-dimensional structure. It can conserve bioactivity (based on a protective membrane structure), enhance biodistribution, and support interactions with target cells mainly in local tissues.[18] Owing its homing ability, exosomes can enter target cells by fusion with the plasma membrane, endocytosis, micropinocytosis, phagocytosis, and lipid raft-mediated internalization.[19] Due to these skill-sets of exosomes, they have been exploited in drug delivery to the tumor where it deserves to recognize cancer and reduces the nonspecific distribution of the drug to a wide range of tissues and organs.[20] Taking advantages of both iRGD and exosomes, the aim of this membrane fusion mediated iRGD-modified liposomes and exosomes formulation is to overcome their respective shortcomings. iRGD-modified liposome shows prominent efficiency for crossing BBB but lacks of capability to target GSCs. On the other hand, exosomes have the advantage of being fused with parental GSCs but only in short distance. While structurally, both iRGD-modified liposome and exosomes are similar having lipid bilayer with ranges in size, exosomes differ from synthetic liposome mainly by the presence of exosome proteins. Therefore, exosomes were hybridized with iRGD-modified liposome to formulate hybrid exosome with uniform size distribution. The aim of using human U87 glioblastoma spheroids as exosome source is to exploit the GSCs targeting characteristic of exosome excreted by GSCs. Align toward this direction, we hypothesize that hybrid exosomes will carry the GSCs targeting properties along with excellent permeated ability across BBB which can be used for GBM-specific therapy.

Herein in this study, fine core-shell nanoparticles, consisting of hollow ZnS nanoparticles covered by dual responsive hybrid exosome shell containing exosome and dual responsive iRGD derived phosphatidylserine, and incorporated with HCQ, denoted as HCQ@ZnS@exo@iRGD, were synthesized to enable pH and redox responsive, H<sub>2</sub>S-sensitized PDT/chemotherapy synergistic therapy. As demonstrated in Figure 1, ZnS core, prepared *via* one-pot hydrothermal method, is camouflaged with exosome excreted by human U87 glioblastoma spheroids. HCQ molecules are incorporated into the hollow ZnS core before the coating procedure (defined as HCQ@ZnS@exo), and subsequently RGD-modified liposome is grafted on the surface of HCQ@ZnS@exo to form HCQ@ZnS@exo@iRGD. iRGD-modified phosphatidylserine acts as a pH and redox-responsive ligand for HCQ@ZnS@exo to

cross BBB and reach GBM site. Owing to high GSH concentration in acidic TME, iRGD shell would be detached and exosome membrane of HCQ@ZnS@exo subsequently is exposed for targetedly fusing with GSCs. Visible light source is used to trigger the ROS induction of hollow ZnS nanopartilces for causing damage to organelles of GSCs. Meanwhile, in acidic condition of lysosome, ZnS core degrades to produce H<sub>2</sub>S gas and release its cargo of HCQ as well *in situ*. The intracellular production of H<sub>2</sub>S does not only exhibit cytotoxicity to the GSCs, but also combined with HCQ to suppress the acidification of lysosome and further blocked the autophagy flux, favoring free radical damage aggregation in cancer cells. The considerable ROS and H<sub>2</sub>S production as well as the suppressed autophagy activity by HCQ, agitates the cytotoxicity of ROS and H<sub>2</sub>S in cascaded manner. Consequently, significant targeted GSCs inhibition is achieved, both *in vitro* and *in vivo*, owing to the combined effects of ROS, H<sub>2</sub>S and autophagy-deactivated activity enabled by HCQ@ZnS@exo@iRGD nanocomposites, indicating its considerable potential for effective GBM treatment.

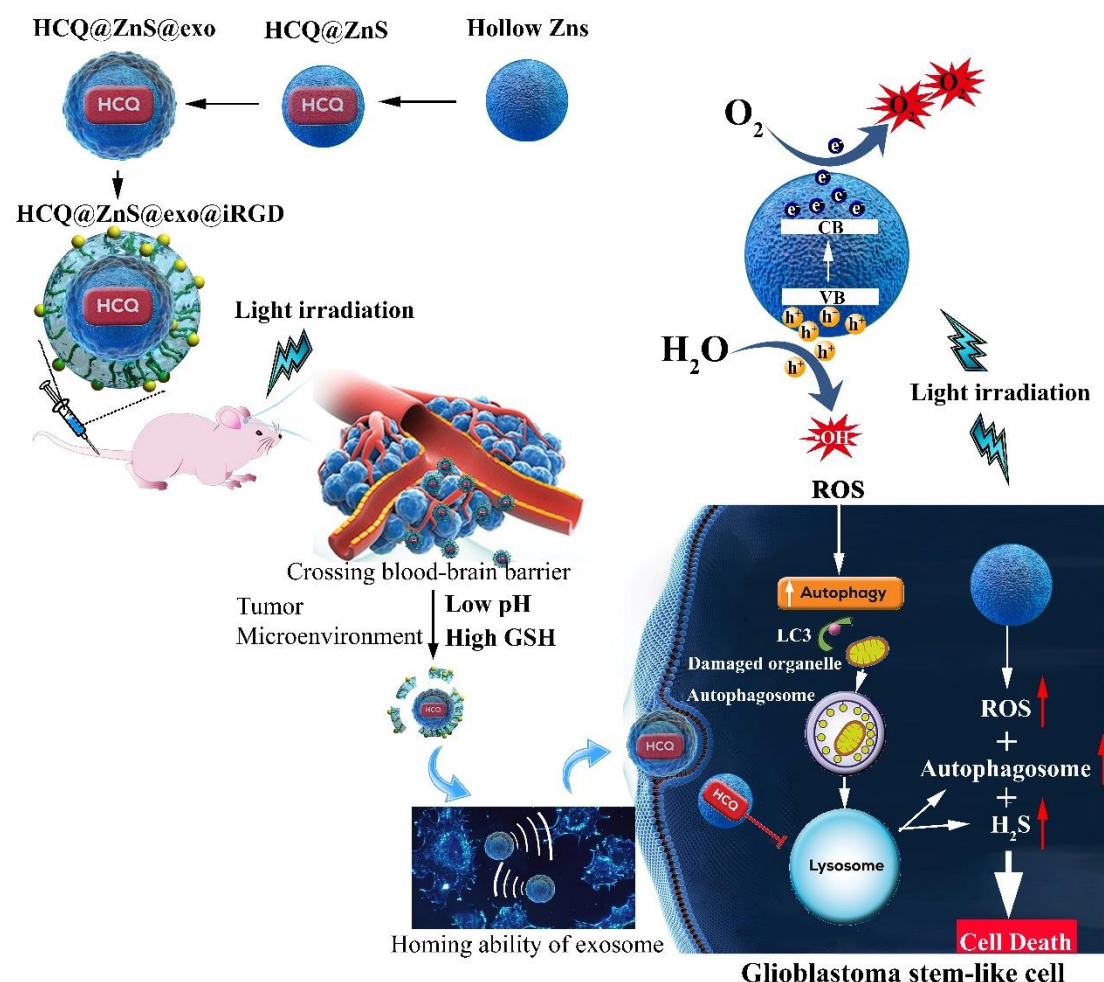


**Figure 1.** Schematic illustration of dual responsive HCQ@ZnS@exo@iRGD as a ZnS-sensitized PDT/chemotherapeutic synergistic nanoplatform for targeted treatment of glioblastoma stem-like cells in orthotopic mouse glioblastoma model.

## 2. Methods

### 2.1. Materials

Zn(Ac)<sub>2</sub>·2H<sub>2</sub>O (AR) and gelatin (GR) were purchased from Aladdin Industrial Corporation (Shanghai, China). CH<sub>4</sub>N<sub>2</sub>S (AR) was purchased from Tianjin Tianli Chemical Reagent Co., Ltd, China. Ethanol (AR) was purchased from Tianjin Kernel Chemical Reagent Co., Ltd, China. Phosphatidylserine and cholesterol were attained from Zhengdong Biotechnology Corporation (Xi'an, China). Hydroxychloroquine sulfate was obtained from MedChemExpress (NJ, USA). All the reagents were used without further purification.

### 2.2. Cell Culture

Human U87 glioblastoma cells were purchased from American Type Culture Collection (ATCC, Manassas, VA). human MCF10A breast epithelial cells were obtained from Shanghai Cell Biology Institute of Chinese Academy of Sciences (Shanghai, China) and cultured in DMEM supplemented with 10% FBS at 37 °C in a humidified atmosphere of 5% CO<sub>2</sub> after receiving. GSC spheres of U87 cells were formed and maintained in suspension in serum-free DMEM/F12 supplemented with N2, G5 and



B27, plus 1% penicillin/streptomycin (ThermoFisher Scientific).[21] Culture supernatants were collected 2 days later and processed for exosome purification by ultracentrifugation steps.[22]

### **2.3. Experimental animal**

Female BALB/c nude mice weighing approximately 20 g were purchased from the Model Animal Research Center of Nanjing University (Nanjing, China). All animal experiments were performed in compliance with the Principles of Laboratory Animal Care (People's Republic of China).

### **2.4. Synthesis of ZnS hollow nanospheres**

In a typical synthesis,  $\text{Zn}(\text{OAc})_2 \cdot 2\text{H}_2\text{O}$  (1 mmol) and  $\text{CH}_4\text{N}_2\text{S}$  (5 mmol) were dissolved in 30 mL distilled water (solution A). Gelatin (0.8780 g) was added to another 30 mL distilled water under vigorous magnetic stirring until the gelatin had dissolved (solution B). The two solutions were mixed and stirred for 10 min before being transferred to a Teflon-lined autoclave (100 mL in volume). The autoclave was heated to 130 °C and kept at 120 °C for 60 h. After cooling to room temperature naturally, the solids were collected by centrifugation, then washed with distilled water and absolute ethanol several times and dried at 60 °C.[23]

### **2.5. ZnS characterization**

X-ray powder diffraction (XRD) patterns were obtained on a Bruker D8 diffractometer using  $\text{Cu K}\alpha$  ( $\lambda = 1.5406 \text{ \AA}$ ) radiation with an accelerating voltage of 40 kV and an applied current of 20 mA. The structure of the samples was analyzed by scanning electron microscopy (SEM: Hitachi S-4800) with an acceleration voltage of 5 kV and transmission electron microscopy (TEM: JEM-2100) with an acceleration voltage of 200 kV. X-ray photoelectron spectroscopy (XPS) analysis was performed on a VG ESCALABMK II with a  $\text{Mg K}\alpha$  achromatic X-ray source (1253.6 eV).

### **2.6. *In vitro* methylene blue dye degraded by ZnS nanoparticles under different pH with/out visible light irradiation**

The methylene blue (MB) dye degraded by ZnS was assayed using a spectrophotometrical procedure that was reported previously with modifications.[24] Briefly, 10 mg of ZnS was immersed in 250 ml of buffer solutions containing MB (2mg/L) with various pH values (pH = 7.4, 6.4, 5.5) with/out visible light irradiation from 600 W tungsten halogen lamp and stirred gently at 37 °C. At each incubation time interval (up to 3 h), 500  $\mu\text{L}$  of sample solution was collected and replaced with fresh buffer solutions of the required pH value. The visible light-vis spectrum of the supernatant was recorded on a visible light-vis spectrophotometer (visible light-2450) to monitor the absorption behavior after centrifugation. The characteristic absorption peak of MB at 664 nm was used to determine the extent of its degradation.

### **2.7. Synthesis of iRGD-derived phosphatidylserine**

Dual responsive iRGD-derived phosphatidylserine (iRGD-PEG-ss-aPS) was synthesized as detailed in *Supplementary Information*. Its chemical structure was confirmed by  $^1\text{H}$ -NMR (Mercury 400, Varian, Palo Alto), FTIR (Spectrum One, Perkin Elmer, Waltham) and ESI-MS (Finnigan TSQ Quantum EMR, Thermo Fisher Scientific Corp., San Jose, USA).

### **2.8. Exosome purification**

Exosomes were isolated from GSC conditional media by using total exosome isolation (from cell culture media) reagent (Invitrogen), according to the manufacturer's instruction.[25] Exosome protein was quantified with Pierce™ BCA protein assay kit (ThermoFisher). The morphology of exosomes was observed by transmission electron microscopy; the size and quantity of particles isolated were examined using a Nanosight NS300 (NanoSight Ltd., Amesbury, UK) and the marker expressions were evaluated by Western blot.

## 2.9. Preparing HCQ@ZnS

HCQ was used as an anticancer model drug and was loaded into the hollow ZnS nanoparticles via physical encapsulation technique. Briefly, 10 mg of ZnS nanoparticles was immersed into an HCQ phosphate buffer solution (pH 7.4) (5 mg/mL, 1 ml) and kept at 37°C for 24 h to achieve the equivalent state. Subsequently, HCQ loaded ZnS nanoparticles (HCQ@ZnS) were collected by centrifugation, washed with pure ethanol for three times to remove the absorbed HCQ at the outer surface of ZnS nanoparticles. HCQ@ZnS was then freeze-dried for next experiments.

## 2.10. Synthesis of exosome coated HCQ@ZnS (HCQ@ZnS@exo)

HCQ@ZnS covered by exosome was synthesized by using simple thin film hydration followed by membrane extrusion as described by Pitchaimani et al with minor modifications.[26] Briefly, 200 mg protein equivalent of purified exosome in 5 mL PBS mixed with 20 mg HCQ@ZnS to form thin film by rotavapor. It was then vortexed and sonicated for proper mixing after hydrated by PBS (pH 7.4). The mixture was extruded using 200 nm polycarbonate membrane filter to get nano-sized HCQ@ZnS@exo, which were collected by centrifugation, washed with PBS (pH 7.4) for three times before freeze-dried for further use.

## 2.11. Synthesis of HCQ@ZnS@exo@iRGD

HCQ@ZnS loaded hybrid Exosomes (HCQ@ZnS@exo@iRGD) were synthesized by simple thin film hydration followed by a membrane extrusion method. Briefly, iRGD-PEG-ss-aPS and cholesterol were dispersed in chloroform in a molar ratio of 2:1 in the round-bottom flask attaching to the rotavapor to form thin film. Previously prepared HCQ@ZnS@exo in PBS were used to hydrate the dry lipid layer containing iRGD-PEG-ss-aPS and cholesterol. Twenty mg protein equivalent of HCQ@ZnS@exo was added to 50 mg of lipid film in a final volume of 5 mL. It was then vortexed and sonicated (30% amplitude, 30 sec pulse on/off, for 2 min) for proper mixing. Thus, formed multilamellar HCQ@ZnS@exo@iRGD solution was extruded through 200 nm polycarbonate membrane filter to get nano-sized HCQ@ZnS@exo@iRGD, which were collected by centrifugation, washed with PBS (pH 7.4) for three times before freeze-dried for further experiments.

## 2.12. Evaluation of Drug loadings and their releasing profile

Quantification of the HCQ for the drug loading and releasing profile were determined using a method based on LC-MS/MS as described in *Supplementary Information*. The drug loading (DL) of HCQ in the freeze-dried nanoparticles powder was calculated using the following equation:



$$DL (\%) = \frac{\text{amount of hydroxychloroquine in freeze-dried nanoparticle } (\mu\text{g})}{\text{amount of freeze-dried nanoparticle } (\mu\text{g})} \times 100\%$$

The entrapment efficiency (EE) was calculated from the following equation:

$$EE(\%) = \frac{\text{amount of hydroxychloroquine in nanoparticle pellet } (\mu\text{g})}{\text{amount of hydroxychloroquine in nanoparticle dispersion } (\mu\text{g})} \times 100\%$$

Drug release study was carried out in physiological (PBS, pH 7.4) or acidic (Acetate buffer, pH 5.5) and/or 20 mM dithiothreitol. 2 mL of 100  $\mu\text{g/mL}$  of HCQ@ZnS@exo@iRGD were immersed in 100 mL of drug release media kept at 37 °C while constant stirring (80 rpm). 500  $\mu\text{L}$  of release media was taken at regular intervals and replaced by fresh media. After centrifugation, the amount of HCQ in the release media was determined by LC-MS/MS as mentioned above.

### 2.13. Characterization of HCQ loaded ZnS nanoparticles

HCQ@ZnS, HCQ@ZnS@exo and HCQ@ZnS@exo@iRGD were characterized for particle sizes and surface charge via TEM and dynamic light scattering assay (DLS, Malvern ZSP). Surface morphology of HCQ@ZnS, HCQ@ZnS@exo and HCQ@ZnS@exo@iRGD were studied using scanning electron microscopy. Protein quantification of exosome and HCQ@ZnS@exo@iRGD were done by using Bradford assay (BioTek, Winooski, USA). Stability of vesicles was studied by monitoring the change in size and PDI for up to 7 days.

### 2.14. Elucidation of hybridization

Validation of hybridization of HCQ@ZnS@exo@iRGD was done by fluorescence resonance energy transfer (FRET) study. FRET has been widely used to study membrane fusion. FRET liposomes were prepared with FRET pairs: 1- $\alpha$ -Phosphatidylethanolamine-N-(4-nitrobenzo-2-oxa-1,3-diazole) (Ammonium salt) (PE-NBD) (Fluorescent donor,  $\lambda_{\text{em}} = 525 \text{ nm}$ ) and 1- $\alpha$ -Phosphatidylethanolamine-N-(lissamine rhodamine-B sulfonyl) (Ammonium salt) (PE-Rh-B) (Fluorescent acceptor,  $\lambda_{\text{em}} = 595 \text{ nm}$ ) (Merck KGaA, Darmstadt, Germany) in 1:7 M ratio. FRET liposomes were synthesized by thin-film method as described in previous research. FRET fluorophore lipids, NBD acting as an electron donor and Rh-B acting as an electron acceptor, resulted in the formation of FRET liposome. For fusion analysis, 100  $\mu\text{L}$  of HCQ@ZnS@exo@iRGD (1 mg/mL) was added to 20  $\mu\text{L}$  FRET liposomes (1 mg/mL), mixed and bath sonicated for 5 min to initiate fusion. FRET liposomes, before and after fusion of HCQ@ZnS@exo@iRGD, were analyzed by fluorescence spectroscopy by exciting samples at 470 nm and measuring the emission spectra between 500 and 700 nm. Protein characterization of parental cells and exosomes and HCQ@ZnS@exo@iRGD were done via SDS-PAGE analysis, Dot blot assay, and western blotting.

For SDS-PAGE analysis, cell lysate, exosomes and HCQ@ZnS@exo@iRGD were

mixed with sample loading buffer (1:1) with a final protein concentration of 200 µg/mL, respectively. The mixture was incubated at 90 °C for 7 min, and 25 µL of each sample was loaded in the wells of 4–20% Mini-PROTEAN® TGX Protein Gels. The gel was stained by Coomassie Brilliant Blue and imaged by Bio-Rad imager.

For Dot blot assay, a drop of each sample (2–3 µL) was added to Polyvinylidene Fluoride (PVDF) membrane. The membrane was incubated with blocking buffer for 30 min at room temperature and then treated with primary antibodies CD81, CD63, CD9, CD11b, TSG101, β-Actin, and histone H3 (Santa Cruz). After overnight incubation with the primary antibody, the membrane was washed with wash buffer and incubated with HRP conjugated anti-mouse IgG secondary antibody (Cell signaling). The membrane was further developed using Signal Fire ECL TM Reagent and immediately imaged by Bio-imager (Kodak).

## **2.15. *In vitro* study**

### **2.15.1. Cellular internalization of HCQ@ZnS@exo@iRGD**

Cellular internalization of vesicles was studied using Confocal Laser Scanning Microscope (Carl Zeiss, LSM-700). 10,000–20,000 U87 cells and MCF10A cells were seeded in 8 well plates for 24 h at 37 °C in 5% CO<sub>2</sub> environment to form mono-layer cells. To form three-dimensional tumor spheroids, U87 cells were seeded at a density of 5×10<sup>3</sup> cells per well in a Corning® 96 Well Ultra Low Attachment Microplate. Cells were incubated with Rh-B labeled formulations for 3 h at 37 °C in 5% CO<sub>2</sub> environment. Cells were then fixed by 4% Paraformaldehyde. Nucleus was stained by DAPI and cells were observed under a Confocal Laser Scanning Microscope. Image-Pro Plus 5.1 software (Media Cybernetics Inc., Rockville, MD, USA) was used to quantify the fluorescent intensity of internalized Rh-B labeled formulations.

### **2.15.2. Expression of mCherry-EGFP-LC3 and GFP-LC3 in U87 cells**

pBABE retroviral vectors containing mCherry-EGFP-LC3 (Addgene, 22418) or GFP-LC3 (Addgene, 22405) were transfected into PT67 cells (ATCC) using Lipofectamine 3000 (Life Technologies).[27] Retrovirus-containing suspension was collected after 48 h, passed through a 45 µm filter to obtain viral particles and U87 were transduced in suspension while spinning at 180 g for 1 h and subsequently selected with puromycin.

### **2.15.3. Fluorescent imaging of lysosomes and autophagosomes**

For visualization of lysosomes and autophagosomes, U87 cells expressing EGFP-LC3 were treated for 3 h with free HCQ, HCQ@ZnS, HCQ@ZnS@exo or HCQ@ZnS@exo@iRGD at 40 µM HCQ and labeled for 15 min with 25 nM LysoTracker Red. The fluorescence signal was examined using confocal microscopy. To quantify lysosome inhibition and autophagosome accumulation in cells, the intensity of lysosomal red fluorescence and the number of green (autophagosomes) puncta were quantified in at least 25 cells. Three independent experiments were performed. Lysosome and autophagosome were quantified using OriginPro 8.0 (Origin Lab Corporation).

### **2.15.4. Monitoring Autophagic flux**

Autophagic flux was determined by confocal microscopic images on ratio of mCherry:EGFP in U87 stably expressing the tandem reporter mCherry-GFP-LC3 after different treatments. Three fields of view were randomly chosen for each group before

Image-Pro Plus 5.1 software was used for quantitative analysis of intensity of fluorescence and number of puncta.

### **2.15.5. Western blotting**

For western blotting, SDS PAGE was run as described earlier.[28, 29] 25  $\mu$ L of samples mixed with sample loading buffer (1:1) containing 25  $\mu$ g protein were loaded in the gel. After the completion of the SDS PAGE, the gel was transferred to PVDF membrane for the transfer of protein by the wet-blot method as described in our recent publications. PVDF membrane was treated with primary antibodies  $\beta$ -Actin and CD9, CD63, HSP 70, LC3-I and II, SQSTM1/p62, GADPH (Santa Cruz) along with HRP conjugated anti-mouse IgG secondary antibody (Cell signaling). The membrane was further developed using Signal Fire ECL TM Reagent and immediately imaged for chemiluminescence by Bio-imager (Kodak).

After treated with free HCQ, HCQ@ZnS, HCQ@ZnS@exo or HCQ@ZnS@exo@iRGD at 40  $\mu$ M HCQ, approximately  $3 \times 10^6$  cells were collected and homogenized with cell lysis buffer containing protease inhibitors (Sigma-Aldrich, MCL1). The protein concentration was determined by Bio-Rad Protein Assay and an equal amount of proteins (20  $\mu$ g) was loaded on precast acrylamide gels (4–12% SDS-PAGE). The gels were transferred to polyvinylidene difluoride membranes, and incubated with primary antibodies at 4°C overnight. The next day membranes were washed with TBS-T solution (Abcam, ab64204) and incubated for 1 h at room temperature with the appropriate HRP-conjugated secondary antibody (ThermoFisher, 32230). The binding was detected by Immobilon Western HRP Substrate (Millipore, WBKLS0100) using the ChemiDoc MP system (Bio-Rad Laboratories, USA). Band intensities were quantified using ImageJ. All antibodies were diluted at 1:1000 in 5% bovine serum albumin (Invitrogen, 15561020) in TBS-T before use.

### **2.15.6. Cytotoxicity evaluation**

Cytotoxicity of different formulations was analyzed on U87 cells using MTT assay. Briefly, 10,000 cells were seeded in 96 well plates for 24 h at 37 °C in 5% CO<sub>2</sub> environment. After that, cells were incubated with free HCQ or different HCQ formulations at varying concentration range (6.25, 12.5, 25, 50, 100, and 200  $\mu$ M) for 48 h with/out visible light irradiation. Control cells were maintained with media only. MTT solution (20  $\mu$ L, 5 mg/mL) was added to each well and cultures were incubated another 4 h. DMSO was added to dissolve the insoluble formazan crystal formed after MTT treatment, and absorbance was recorded at 550 nm using microplate reader (BioTek, Synergy H1 Hybrid reader). IC<sub>50</sub> values were determined from these absorbance measurements.

### **2.15.7. Caspase 3/7 activity assay**

Caspase 3/7 activity was performed using the Caspase-Glo 3/7 Assay (Promega) according to the manufacturer's protocol. Cells were treated with different formulations and assayed after 24 h. Briefly, plates and reconstituted caspase 3/7 reagent were allowed to equilibrate to room temperature (RT), reagent was then added to wells at a 1:1 ratio and incubated for 1 h at RT. Images of cells were taken by CLS. Wells with all assay components, except the cells, served as blank controls.

### **2.15.8. Effect of HCQ@ZnS@exo@iRGD on 3 D tumor spheroids**

BT-549 cells were allowed to form 3 D spheroids by seeding them at a density of  $5 \times 10^3$  cells/100  $\mu$ L per well in a Corning® 96-Well Ultra-Low-Attachment Microplate and incubating them for several days. 3D spheroids were incubated for 24 h in culture medium containing free HCQ, different HCQ nanoparticles or PBS (control). Then supernatants were aspirated, fresh standard medium was added and cells were further cultured for another 5 days. On day 5, spheroids were photographed using phase-contrast microscopy.

## **2.16. *In vivo* study**

### **2.16.1. Establishment of orthotopic glioblastoma xenograft in BALB/c nude mice**

The orthotopic mouse glioblastoma model were established through intracranial implantation of U87 cells as previously reported.[30] Briefly,  $2 \times 10^5$  U87 cells expressing luciferase (Luc-U87) were injected intracranially into the frontal lobes of BALB/c nude mice. The stereotactic coordinate of the injection spot on the mice was 0.5 cm posterior to the frontline, 0.5 cm to the left of the middle and 0.5 cm below the skull. Multiple holes were drilled around the injection site allowing for light penetration. The growth of an orthotopic tumors were detected and quantified by bioluminescence imaging performed in an *In Vivo Image System* (IVIS) Spectrum (PerkinElmer, USA) by intraperitoneal injection of D-luciferin potassium salt (150 mg/kg).

### **2.16.2. Different formulations' distribution in glioblastoma bearing mice model**

The mice bearing orthotopic glioblastomas were given free Cy 5.5, Cy 5.5@ZnS, Cy 5.5@ZnS@exo or Cy 5.5@ZnS@exo@iRGD via tail vein injection. (n=3) The mice were then subjected to IVIS imaging system at various time points, revealing by the red fluorescence of Cy 5.5. At 24 h post-injection, the mice were sacrificed. Major organs and brain were obtained for fluorescent imaging.

### **2.16.3. Anti-glioblastoma, anti-stemness and pro-apoptosis effects**

The mice bearing intracranial Luc-U87 glioblastoma were randomly divided into 5 groups (n = 9), and tail intravenously administered with free HCQ, HCQ@ZnS, HCQ@ZnS@exo or HCQ@ZnS@exo@iRGD with/out light irradiation and saline, respectively. The growth of the orthotopic glioblastoma was detected by the luciferin for *in vivo* imaging. (n=6) The injection treatment was carried out every 3 days for a total of eight injections. Six hours later after the injection, the tumor sites in the mice head were locally irradiated by 500 W tungsten halogen lamp for 10 min. Meanwhile, the body weights of the mice were weighted every 3-4 days. The survival times were calculated since the glioblastoma inoculation to the day of death or until the day 80, and the statistical difference was plotted by the Kaplan-Meier method.

Anti-stemness and pro-apoptosis effects of free HCQ, HCQ@ZnS, HCQ@ZnS@exo or HCQ@ZnS@exo@iRGD with/out light irradiation and saline on glioblastoma mice model was studied by immunofluorescence and viewed under confocal microscopy. (n=3) On the day 14, mice were euthanized. Tumors were cut into slices 5.0  $\mu$ m thick, rinsed with PBS three times, incubated in binding buffer and stained with annexin V and propidium iodide (Lianke Technology, Hangzhou, China) for 15 min at 25 °C under low-light conditions. Samples were washed again, stained with 5 mM DAPI. Tumor slices were also subjected to antigen retrieval in a pressurized heating chamber (Pascal, Dako, Denmark) in tris-EDTA (pH 9) at 115 °C for 60 s before incubation with primary

antibodies against CD133 and CD90, which are stemness-related markers of GBM. Slices are analyzed under a confocal microscope (Leica TCS SP5, Germany).

### 2.17. Statistical analysis

Differences were assessed for significance using Student's *t* test between two treatment groups or one-way analysis of variance among multiple groups. Three significance levels were reported: \**P* < 0.05, \*\**P* < 0.01 and \*\*\**P* < 0.001.

## 3. Result

### 3.1. Characterizations of ZnS

ZnS was obtained by hydrothermal reaction of Zn(OAc)<sub>2</sub> and thiourea in the presence of gelatin at 130 °C for 60 h (mass ratio of gelatin and Zn(OAc)<sub>2</sub>·2H<sub>2</sub>O is 4 : 1). Fig. 2a shows the XRD pattern of the ZnS sample. Three peaks can be observed at  $2\theta = 28.8^\circ$ ,  $48.4^\circ$ ,  $57.4^\circ$ , which can be indexed to (002), (110) and (112) diffraction peaks of the hexagonal zinc sulfide (No. 80-0007). No other impurity peaks are found. It can also be seen that the diffraction peak of (100) overlaps with the diffraction peak of (002) due to widening of these peaks, implying the small crystallite size of ZnS grains. The morphology of the sample is observed by SEM and TEM analysis. From the SEM image (Fig. 2b), we can see that the ZnS sample is composed of uniform nanospheres with a size of about 81 nm. The nanospheres are well dispersed with no obvious signs of aggregation. The low magnification TEM (Fig. 2c) reveals the spheres possess a coarse surface with a dark edge and a pale center, which confirms the formation of hollow structures. The amplified TEM image (Fig. 2d) further demonstrates the hollow structure of ZnS. The high resolution TEM (HRTEM) image shows the lattice fringe spacings at about 0.31 nm, corresponding to the planar distance of the (002) plane of hexagonal ZnS (Fig. 2d and inset).

The chemical state of the elements in ZnS sample was investigated by X-ray photoelectron spectroscopy (XPS). The wide XPS scan spectrum (Fig. 2e) shows that except for Zn and S elements, the peaks of O, N, C elements can also be observed. The atomic concentration percentage of ZnS is shown in Table S1. The abundant N and C elements in ZnS should derive from surface-absorption species released by gelatin. As shown in Fig. 2f, the binding energies (BE) of Zn2p<sub>3/2</sub> and Zn2p<sub>1/2</sub> peaks in ZnS are about 1021.4 eV and 1044.5 eV, respectively, which are in accordance with the BE values of Zn<sup>2+</sup> in ZnS.[31] Furthermore, the peaks of S2p<sub>3/2</sub> and S2p<sub>1/2</sub> located at 161.9 eV and 163.5 eV (Fig. 2g), are consistent with S<sup>2-</sup> in ZnS. The peak of N1 s can be deconvoluted into two peaks located at about 400.0 eV and 401.5 eV, which can be ascribed to the pyridine-*N* and quaternary-*N* determined by the structure of gelatin itself. (Fig.2h)

### 3.2. *In vitro* methylene blue dye degraded by ZnS nanoparticles

The absorption spectra of MB solutions with/out ZnS nanoparticles under different circumstances for 1 hour are shown in Fig. S1. As can be seen from the spectra, the peak of MB at 664 nm varied significantly after 1 hour under different test conditions. The profile of MB degraded by the ZnS investigated at different pH values with/out light illumination was shown as Fig.2i. Under neutral conditions, the mean percentage degradation of MB was 2.3 % after the first 20 mins and 20.8 % after 3 h. In comparison,

under acidic conditions (designed to simulate the mild acid tumor microenvironment) the mean percentage degradation of MB after 3 h reached 58.4 % and 98.6 % at pH = 6.4 and pH = 5.5, respectively (Fig. 2i). These results demonstrate that, in the presence of hydrogen ions ( $H^+$ ), ZnS nanoparticles of ZnS could react with  $H^+$  to produce  $H_2S$  gas which is a prerequisite for  $H_2S$ -enhanced chemotherapy. Notedly, under visible light illumination, the degradation of MB was significantly increased due to the high photocatalytic performances of ZnS. It is clearly seen that under pH 5.5 only one hour of light irradiation, MB conversion is to reach 94.6 %.



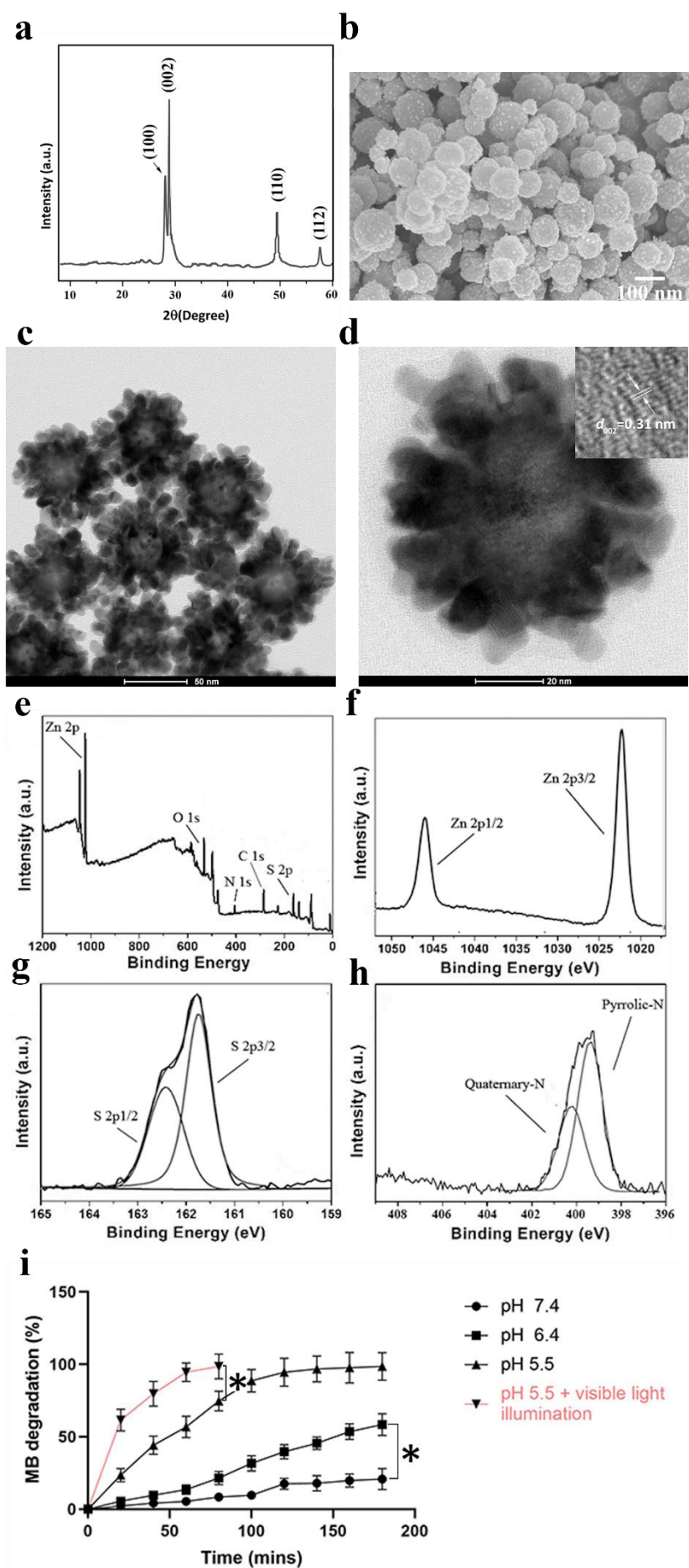


**Figure 2.** (a) XRD pattern, (b) SEM image, (c) TEM and (d) HRTEM images of ZnS. (e) The wide scan XPS spectrum and (f) Zn 2p, (g) S 2p and (h) N 1s spectra of ZnS sample. (i) The profile of MB degradation when co-incubated with the ZnS nanoparticles was investigated at different pH values with/out light illumination. Data shown are mean  $\pm$  SD of 3 replicates. \*,  $p < 0.05$ .

### 3.3. Characterizations of iRGD-PEG-ss-aPS

The  $^1\text{H}$  NMR spectrum of iRGD-PEG-ss-aPS in  $\text{D}_2\text{O}$  were in accordance with the expected structures. As shown in Fig.3a, the signals at 5.08 ppm (peak b) corresponded to the ethenyl protons in phosphatidylserine, which indicated that PS (phosphatidylserine) was successfully activated. The signals at 6.37 ppm (peak a) corresponded to the methylene protons in aconitic anhydride as acid cleavable linker. Protons in PEG chain was observed at 3.45 ppm (peak d). Finally, peak c ( $\delta=5.30$  ppm) was allocated as protons in characteristic methine of iRGD.

The characteristic peaks of PEG linker, phosphatidylserine and iRGD peptides were also observed in the FTIR spectra of final product of iRGD-PEG-ss-aPS. (Fig.3b) Specifically, PEG shows characteristic stretching frequencies for  $-\text{CH}_3$  symmetric, and C–O, at  $2868$  and  $1061\text{ cm}^{-1}$ , respectively. The peaks at  $1,672$  and  $1,540\text{ cm}^{-1}$  were assigned to amide bands from iRGD. After conjugating iRGD with phosphatidylserine *Cis*-aconitic anhydride Cystamine PEG (PEG-ss-aPS), the obvious characteristic amide bands with a slight blue shift ( $1,625$  and  $1,503\text{ cm}^{-1}$ ) with intensified absorption were also observed, indicating the successful conjugation of acid and redox cleavable PEGylated phosphatidylserine with iRGD by the amide bond. The peak at  $1063\text{ cm}^{-1}$  characteristic of the  $\nu_3$  band of  $\text{HPO}_4^{2-}$  are observed in both spectrum of phosphatidylserine and iRGD-PEG-ss-aPS. Therefore, the designated product as iRGD-PEG-ss-aPS was successfully synthesized, as demonstrated in the FTIR spectra. The successful synthesis of iRGD-PEG-ss-aPS was further confirmed by electrospray ionization mass spectrometry (ESI-MS) with a peak at  $[3253.7996\text{ m/z}]$  as its molecular ion peak ( $[\text{M}+\text{H}]^+$ calculated  $[3253.1226\text{ m/z}]$ ) and another characteristic peak at  $[3287.7738\text{ m/z}]$  corresponds to the  $[\text{M}+\text{NH}_4]^+$  ion (calculated  $[3271.3238\text{ m/z}]$ ). (Fig.S2.)

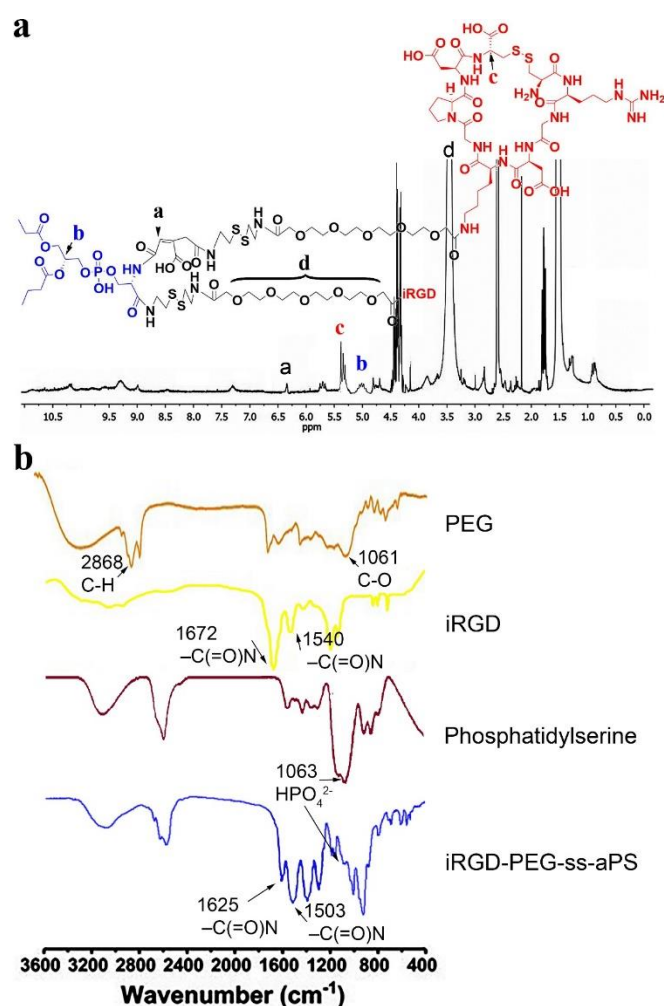


**Figure 3.** Chemical structure of iRGD-PEG-ss-aPS was confirmed by (a) <sup>1</sup>H NMR and (b) FTIR spectrum.

### 3.4. Characterizations of HCQ@ZnS, HCQ@ZnS@exo and HCQ@ZnS@exo@iRGD

The products of HCQ@ZnS, HCQ@ZnS@exo and HCQ@ZnS@exo@iRGD were characterized for size, surface property, and protein content. A comprehensive result on the size distribution and zeta potential along with EE and DL of these nanoparticles was listed in Table 1. Particle sizes of HCQ@ZnS and HCQ@ZnS@exo was found to be  $81 \pm 6.9$  nm (PDI =  $0.17 \pm 0.04$ ) (Fig.4a) and  $99 \pm 9$  nm (PDI =  $0.21 \pm 0.02$ ) (Fig.4b) with zeta potential of  $2 \pm 0.4$  and  $-15 \pm 1$  mV, respectively. Whereas that of HCQ@ZnS@exo@iRGD was found to be  $137 \pm 20$  nm (PDI =  $0.23 \pm 0.04$ ) (Fig.4b) and  $-36 \pm 3$  mV. While there is not much variation in the hydrodynamic size of HCQ@ZnS@exo when extruded through 200 nm polycarbonate membrane, the size of HCQ@ZnS@exo@iRGD was found to be increased to 137 nm. The increase in the size of HCQ@ZnS@exo@iRGD is probably due to the insertion of exosome into the bilayer of synthetic liposome which increases the interaction points of water molecule thereby increasing the hydration layers. Although the size of HCQ@ZnS@exo@iRGD is larger than HCQ@ZnS and HCQ@ZnS@exo, the most important factor is the homogeneity in the size distribution, which can be indexed by determining the polydispersity index (PDI). PDIs of three formulations are bellowed 0.3, which indicated fairly good size

homogeneity of these formulations.

TEM images showed a morphological characteristic of these nano-sized particles for HCQ@ZnS@exo (Fig.4c) and HCQ@ZnS@exo@iRGD (Fig.4d). These images of HCQ@ZnS@exo and HCQ@ZnS@exo@iRGD were compared for morphological analysis, which exhibited a clear distinction between the nanoformulations. HCQ@ZnS@exo@iRGD with the dense network around the surface which may be due to hybridization of PEG chain and iRGD peptide with the exosome. Likewise, in SEM images, HCQ@ZnS@exo@iRGD (Fig.4f) showed distinct different surface morphology than that of HCQ@ZnS@exo (Fig.4e).

To further examine the stability of these nanoparticles, we monitored their colloidal stability up to 7 days as depicted in Fig. 4g and h. HCQ@ZnS@exo@iRGD showed better stability compared to HCQ@ZnS@exo and HCQ@ZnS, both in terms of PDI and particle sizes. During the period of 7 days, PDI of HCQ@ZnS@exo@iRGD varied from 0.17 to 0.25 compared to 0.17 to 0.68 and 0.22 to 0.28 for HCQ@ZnS and HCQ@ZnS@exo, respectively. These characterization data show that incorporation of the lipid layer of the liposome with exosome in HCQ@ZnS@exo@iRGD results in better stability of engineered HCQ@ZnS@exo@iRGD compared to naive exosome covering HCQ@ZnS.

### 3.5. Hydroxychloroquine loading and release study

Next, we studied the drug loading and release kinetics to explore the potential application of ZnS@exo@iRGD in drug delivery. HCQ was loaded in ZnS@exo@iRGD using membrane extrusion mediated physical method of drug loading. Encapsulation efficiency (EE) and drug loading (DL) of HCQ in different formulation were listed in Table 1. EE and DL of HCQ@ZnS were firstly calculated, respectively, as  $27.10 \pm 2.21\%$  and  $15.20 \pm 2.31\%$ . Almost no HCQ leakage from ZnS was observable, as EEs of HCQ@ZnS@exo and HCQ@ZnS@exo@iRGD are as high as 97.5%.

With the assurance of good stability of HCQ@ZnS@exo@iRGD, we further studied drug release to explore the release kinetics at normal physiological pH (pH 7.4, PBS) and acidic (pH 5.5, Acetate buffer) as depicted in Fig. 4i. HCQ@ZnS@exo@iRGD showed similar bursts release in both pH conditions up to the first 8 h, with enhanced drug release characteristic in acidic pH compared to physiological pH when evaluated for 48 h. The initial burst release of the drug was found to follow first order release kinetics model ( $R^2$  of 0.96 and 0.98). After the initial burst release, pH-responsive release characteristic was observed up to 48 h in pH 5.5. Besides pH sensitive feature, higher release from HCQ@ZnS@exo@iRGD was also found under high GSH, which may attribute to redox-cleavable bond of HCQ@ZnS@exo@iRGD outer layers. Overlapping these two factors together would lead to much steeper releasing curve. As shown in red curve in Fig.4i, the accumulative release of HCQ will reach plateau of 95% within just 24 h.

All in all, our formulated HCQ@ZnS@exo@iRGD showed a precisely controlled trend of drug release characteristic signifying that this engineering nanoparticles may be applied to complex tumor microenvironments.

**Table 1.** Physical characterizations of different ZnS based nanoparticles.

<b>Sample</b>	<b>Diameter r [nm]<sup>a</sup></b>	<b>PDI<sup>a</sup></b>	<b>Zeta potential [mV]<sup>a</sup></b>	<b>EE [%]<sup>b</sup></b>	<b>DL [%]<sup>b</sup></b>
<b>ZnS</b>	82±18.0	0.19±0.03	0.33±0.29	N.A.	N.A.
<b>HCQ@ZnS</b>	81 ± 6.9	0.17 ± 0.04	2 ± 0.4	27.10±2.21	15.20±2.31
<b>HCQ@ZnS@ exo</b>	99 ± 9	0.21 ± 0.02	-15 ± 1	97.52±5.6	6.45±1.85
<b>HCQ@ZnS@ exo@iRGD</b>	137 ± 20	0.23 ± 0.04	-36 ± 3	95.78±6.6	3.04±0.54

DL: drug loading; EE: encapsulation efficiency; PDI: polydispersity index;

N.A. not applicable

n=5, mean±SD

<sup>a</sup> Based on dynamic light scattering

<sup>b</sup> Based on Lc-Ms/Ms



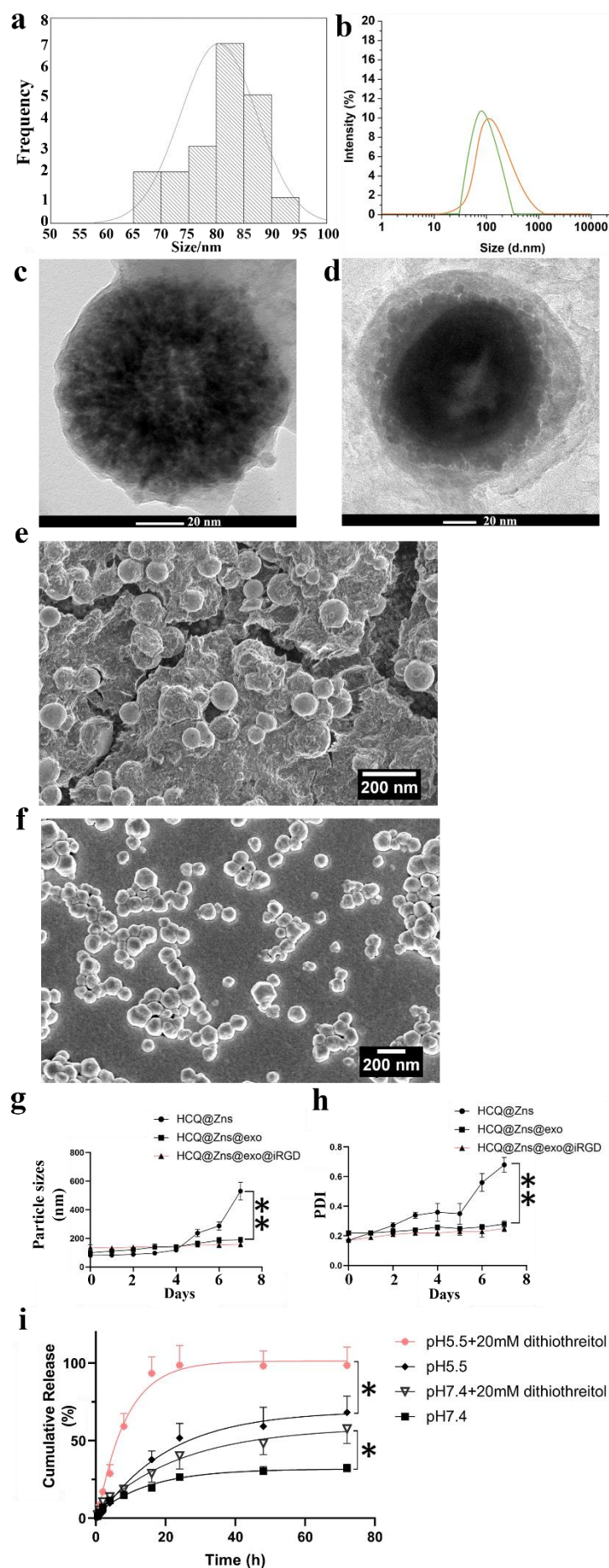




**Figure 4.** Characterizations of ZnS based nanoparticles. Particle sizes distribution of (a) HCQ@ZnS, (b) HCQ@ZnS@exo and HCQ@ZnS@exo@iRGD; Transmission electron microscope image of (c) HCQ@ZnS@exo and (d) HCQ@ZnS@exo@iRGD; Scanning electron microscope image of (e) HCQ@ZnS@exo and (f) HCQ@ZnS@exo@iRGD; Stability of nanoparticles over 7 days in terms of (g) particle sizes and (h) PDI, respectively. (i) *In vitro* drug release study. Percentage release of (HCQ) hydroxychloroquine from HCQ@ZnS@exo@iRGD in different circumstances. Data shown are mean  $\pm$  SD of 3 replicates. \*,  $p < 0.05$ , \*\*,  $p < 0.01$ .

### 3.6. Validation of hybridization

Fluorescence resonance energy transfer (FRET) and protein assay were carried out for the confirmation of hybridization between liposome and hybrid exosome.[32] Energy transfer in FRET liposome was monitored before and after hybridization as depicted in Fig. 5a. Liposome spectra represent before hybridization, and HCQ@ZnS@exo@iRGD spectra represent after hybridization. A diminished FRET effect was seen after hybridization which can only happen when the distance between the FRET pair increases. This suggests that there has been the insertion of exosome content in the lipid bilayer of liposome validating successful hybridization, which confirmed the successful formation of HCQ@ZnS@exo@iRGD.

Hybridization was also confirmed by protein characterization. Protein cargo of exosomes is important for their unique characteristic. Sodium dodecyl sulfate–polyacrylamide gel electrophoresis (SDS-PAGE) analysis showed distinct protein bands in both exosome and HCQ@ZnS@exo@iRGD as shown in Fig. 5b. Samples were concentrated to get higher signal intensity. ZnS@exo@iRGD showed similar protein bands like that of exosome, signifying that the exosome protein content has been conserved through the hybridization. More importantly, Dot-blot assay showed the presence of major exosome marker proteins like transmembrane proteins (CD81, CD63, and CD9), tumor susceptibility gene 101 protein (TSG101) (Fig. 5c).[33] These proteins were present in both exosomes and HCQ@ZnS@exo@iRGD, suggested the successful retention of major exosome proteins through hybridization process in HCQ@ZnS@exo@iRGD. The slight decrement of intensity in blot signal in case of HCQ@ZnS@exo@iRGD may be due to the interference by synthetic lipid content of HCQ@ZnS@exo@iRGD (exosome: Lipid = 1:5 in HCQ@ZnS@exo@iRGD).

To further confirm the presence of exosome marker protein in exosomes and HCQ@ZnS@exo@iRGD, one of the major and widely used exosome marker protein CD63 was chosen and analyzed via western blotting. As shown in Fig.5d, western blot assay also confirmed the presence of exosome special marker CD9 and HSP70 in HCQ@ZnS@exo@Irgd confirming our claim.[34]  $\beta$ -actin was used as positive control and histone H3, a nuclear protein was used as a negative control in dot blot study. All three nanoparticles studied showed the presence of  $\beta$ -actin. However, the nuclear protein histone H3 was not present in exosome and HCQ@ZnS@exo@iRGD, which also suggests that the isolated exosomes are free from possible nuclear contamination. Result of both positive and negative control confirms the specificity of the assay performed. These analyses further support the successful fabrication of HCQ@ZnS@exo@iRGD with the conservation of characteristic exosome protein

cargoes.

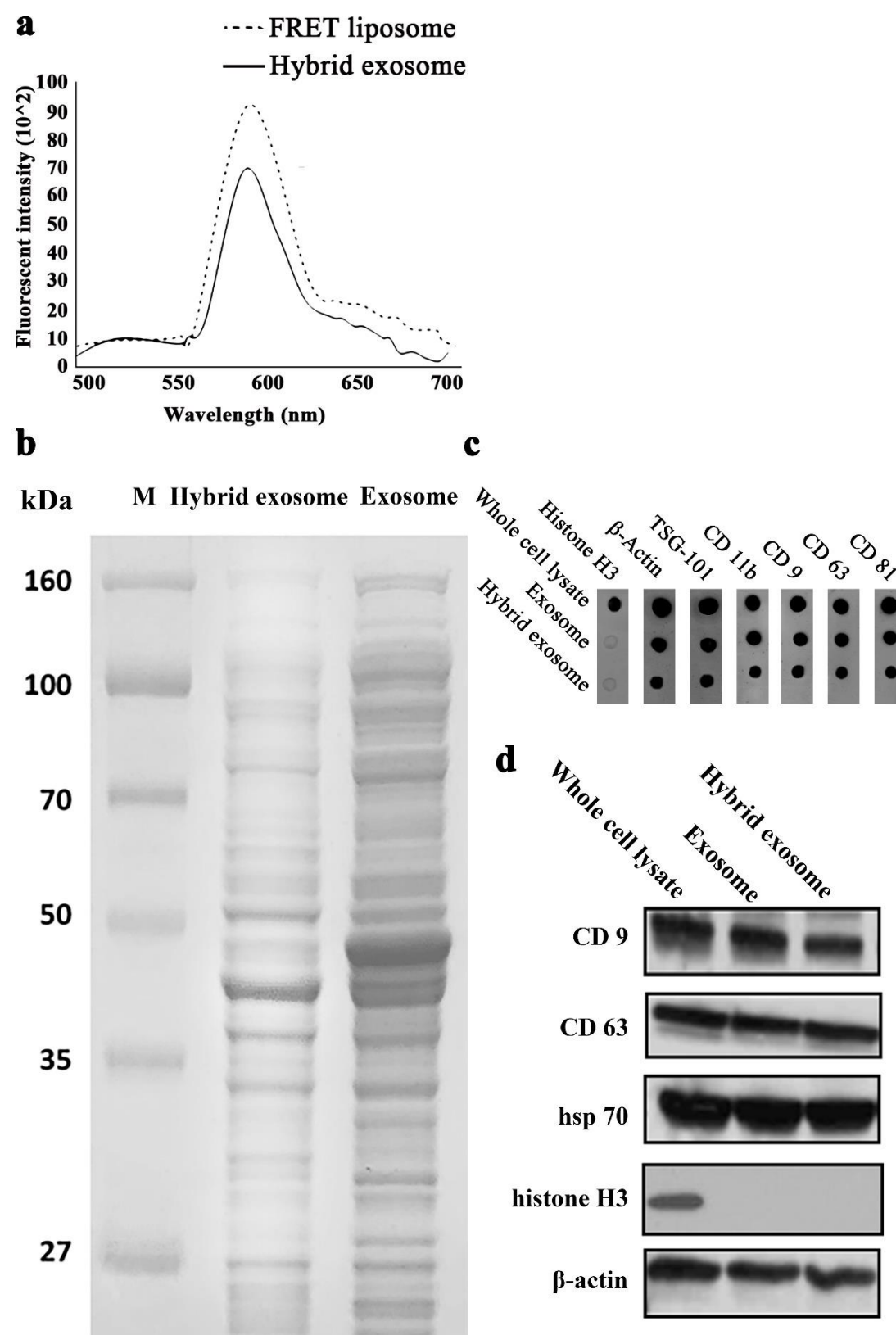


**Figure 5.** Validation of hybrid exosome formation. (a) Fluorescence Resonance Energy Transfer (FRET) study showing successful hybridization of exosome and liposome.

FRET study was conducted using fluorescent donor NBD ( $\lambda_{em} = 525$  nm) and fluorescent acceptor RhB ( $\lambda_{em} = 595$  nm) at excitation wavelength of 470 nm; **(b)** SDS-PAGE analysis of exosome and HCQ@ZnS@exo@iRGD. Both samples were concentrated to get distinct protein bands, **(c)** dot blot assay, and **(d)** western blot assay for the identification of exosome marker proteins in whole cell lysate (WCL), small extracellular vesicle (exosome), and hybrid exosome (HCQ@ZnS@exo@iRGD).  $\beta$ -actin was used as a positive control and histone H3 was used as negative control.

### 3.7. Cellular internalization study

Cellular internalization of HCQ@ZnS@exo@iRGD was studied on Human U87 glioblastoma cells and human MCF10A breast epithelial cells using confocal imaging. Fig. 6 shows confocal imaging of different cell lines showing internalization of Rhodamine-B (Rh-B) labeled formulations and their subsequent quantification after 3 h of treatment. Nanovesicles were stained with Rh-B dye and nucleus of the cell was stained by 4',6-diamidino-2-phenylindole (DAPI). Rh-B fluorescence intensity in the individual cell was quantified using Image-Pro Plus 5.1 software. Untreated cells were used as control. Significant higher cellular internalization of Rh-B@ZnS@exo and Rh-B@ZnS@exo@iRGD compared to Rh-B@ZnS was observed in exosome parent cells U87, whereas the uptake are quite low in normal fibroblast MCF10A cells for all treatment groups ( $p < 0.0001$ , Unpaired *t*-test) and there was no significant uptake difference among treatment groups in MCF10A cells. (Fig. 6a and b) ZnS@exo@iRGD differs from ZnS nanopartilces by the presence of characteristic exosome surface proteins and iRGD. Quantitative measurements of the fluorescence intensity of U87 (Fig.6c) and MCF10A (Fig.6d) cell monolayer showed highest internalization levels of Rh-B@ZnS@exo and Rh-B@ZnS@exo@iRGD by U87 cells, which were consistent with the results of Fig. 6a and b.

The uptake of the cell monolayer shown above might not exactly imitate the behavior of the nanoparticles within the solid tumor due to more complex situations such as modest drug permeation, distorted enzyme activities, and escalated oxygen tension present in the solid tumor.[35] To mimic that actual situation, 3D tumor spheroids were constructed to investigate the uptake of the nanoparticles. The distributions of Rh-B@ZnS in U87 tumor spheroids were weak, indicating Rh-B@ZnS had difficulties in diffusing into hidden territories of the tumor spheroid. In contrast, the fluorescence intensity of Rh-B@ZnS@exo is high especially in the core of U87 tumor spheroids (Fig. 6e). Similarly, the distribution of Rh-B@ZnS@exo@iRGD significantly increased in spheroid, indicating that particles with hybrid liposome may help penetrate into the tumor spheroids (Fig. 6e). Quantitative measurements of the fluorescence intensity of U87 tumor spheroids confirmed the penetrating efficiency of Rh-B@ZnS@exo and Rh-B@ZnS@exo@iRGD (Fig. 6f) and this was consistent with the results of Fig. 6e.

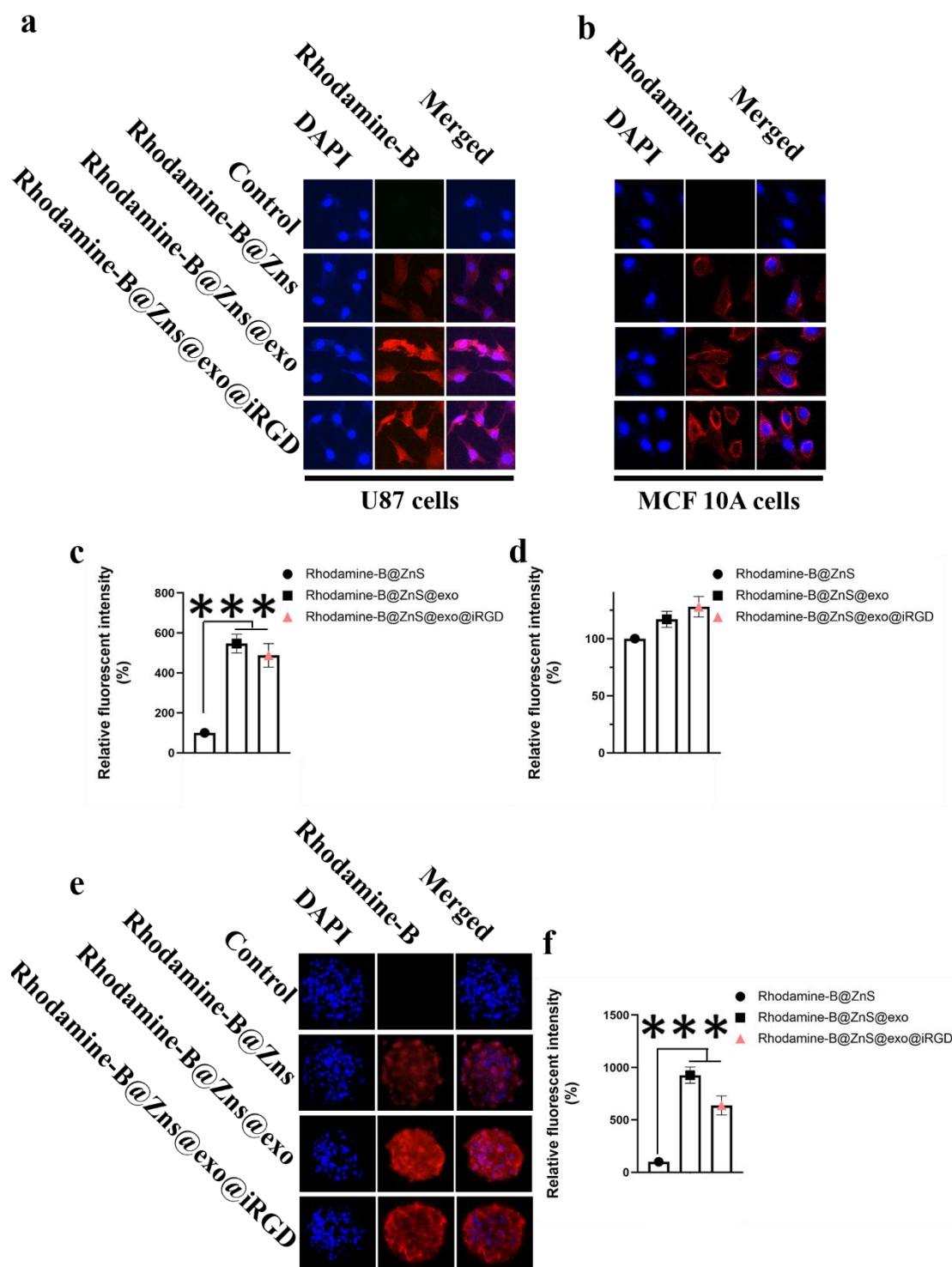


**Figure 6.** Cellular uptake behavior of the Rhodamine-B loaded ZnS nanoparticles. Cellular uptake of different Rhodamine-B formulations in mono-layer of (a) U87 and (b) MCF10A cancer cells observed via confocal microscopy; (Magnification, 500×) Comparison of fluorescent intensities in (c) U87 and (d) MCF10A cells. *In vitro* (e) uptake behavior and (f) quantification of different Rhodamine-B loaded ZnS nanoparticles in U87 tumor spheroids. (Magnification, 200×) Internalization was quantified in terms of fluorescent intensity using Image-Pro Plus 5.1 software. Data shown are mean  $\pm$  SD of 3 replicates. \*\*\*,  $p < 0.001$ .

### 3.8. Lysosome inhibition and autophagosome accumulation in cells

Since HCQ inhibits autophagy by blocking lysosomal degradation, we treated cells with free HCQ, HCQ@ZnS, HCQ@ZnS@exo or HCQ@ZnS@exo@iRGD at pH 7.4 and with LysoTracker Red to specifically mark acidic vesicles within cells. U87 cells treated with HCQ@ZnS@exo and HCQ@ZnS@exo@iRGD showed fewest lysosomal red puncta than other treated groups. (Fig. 7a) To compare the ability of free HCQ, HCQ@ZnS, HCQ@ZnS@exo or HCQ@ZnS@exo@iRGD to inhibit autophagy. Further investigation of the occurrence of autophagy in U87 cells was performed by analyzing the expression pattern of Microtubule-associated protein 1 A/1B-light chain 3 (MAP1LC3, also known as LC3) in U87 cells. Consistent with results of Lysosome inhibition, U87 cells showed increased expression of LC3 over time. Green fluorescence was more obvious with HCQ@ZnS@exo or HCQ@ZnS@exo@iRGD than with free HCQ or HCQ@ZnS.

Validation of autophagy in U87 cells was demonstrated using a tandem fluorescent-tagged LC3B reporter containing mCherry and EGFP (mCherry-EGFP-LC3) that allows real time monitoring of autophagic flux in live cells (Fig. 7b). Yellow LC3 puncta (early autophagosomes not yet fused with lysosomes) were detected in 89.73% or 81.25% of U87 cells at HCQ@ZnS@exo or HCQ@ZnS@exo@iRGD groups of culture. This percentage dropped down to 13.12% at free HCQ treatment group, at which time 86.75% of U87 cells exhibited red-only fluorescent puncta (mature autolysosomes) (Fig. 1d). We conclude that HCQ@ZnS@exo and HCQ@ZnS@exo@iRGD treatments could effectively block autophagy flux.

As a further check on autophagy inhibition, levels of LC3 and SQSTM1/p62, both of which play key roles in autophagy, were measured using western blotting. Increases in the ratio of LC3-II to LC3-I indicate autophagy inhibition, and HCQ@ZnS@exo and HCQ@ZnS@exo@iRGD caused a larger increase than free HCQ or HCQ@Zns after 3 h treatment at a dose of 40  $\mu$ M HCQ (Fig. 7f). SQSTM1/p62 expression was higher with HCQ@ZnS@exo and HCQ@ZnS@exo@iRGD than the other treatments, confirming stronger autophagy inhibition (Fig. 7e).



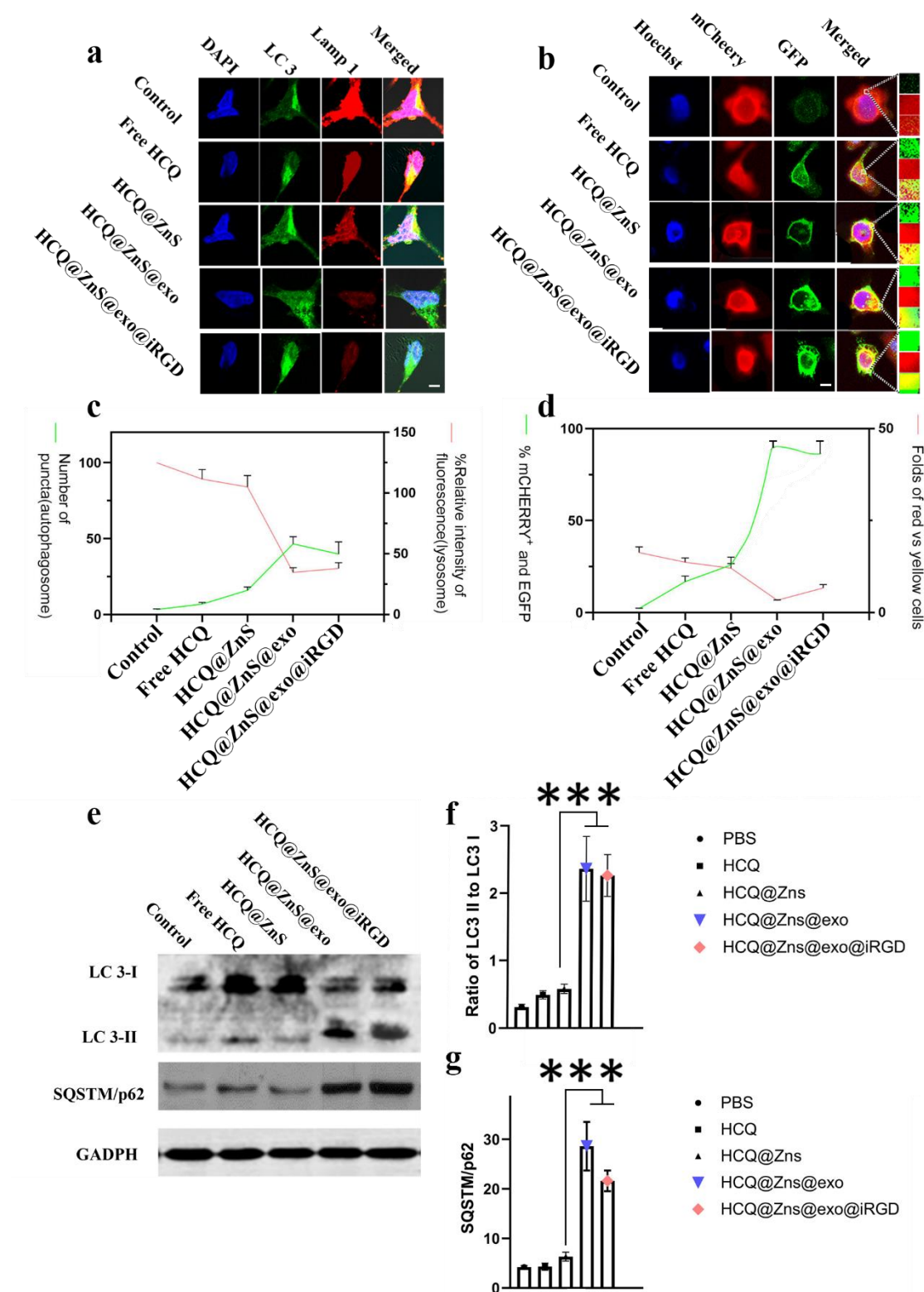


**Figure 7.** U87 cells deactivate autophagy upon HCQ@ZnS@exo@iRGD administration. Representative images are shown for (a) Immunofluorescent staining of lysosomal (LAMP1, red) and autophagic (LC3, green) markers of U87 cells after treated with free HCQ, HCQ@ZnS, HCQ@ZnS@exo or HCQ@ZnS@exo@iRGD (b) The average number of LC3 puncta per cell (mean  $\pm$  SD, n = 30-45 cells) and the relative level of lysosomal puncta compared to the control group. (c) U87 cells



transfected with the mCherry-GFP-LC3 reporter show deactivation and incompleteness of the autophagic cycle (yellow fluorescence) when treated with HCQ@ZnS@exo@iRGD. (d) The graphs represent the percentage of cells with double-positive puncta (mCherry<sup>+</sup> and GFP<sup>+</sup>) (autophagosomes) out of the total number of cells analyzed (left graph) (mean  $\pm$  SD,  $n = 30-39$  cells). And the rate of conversion from cells exhibiting red-only puncta to yellow puncta expressed as fold change (right graph). Autophagy inhibition evaluation of HCQ@ZnS@exo@iRGD. (e) Western blotting for LC3 and SQSTM1/p62. (f) Quantification of the ratio of LC3-II to LC3-I expression using ImageJ software. (g) Quantification of levels of SQSTM1/p62 normalized to those in PBS-treated cells using ImageJ. Scale bars are 5  $\mu$ m for (a) and 10  $\mu$ m for (b). Data shown are mean  $\pm$  SD of 3 replicates. \*\*\*,  $p < 0.001$ .

### 3.9. Autophagy inhibition decreases viability and stemness of U87 cells

To verify the cytotoxic effects of HCQ@ZnS@exo@iRGD, the *in vitro* antitumor effects of free drugs and drug-loaded nanoparticles against U87 cells were tested using MTT assay. We observed a significant increase in the percentage of dead U87 cells, when the treatment with HCQ@ZnS@exo was initiated, compared with those of free HCQ and HCQ@ZnS. Likewise, the number of viable cells decreased significantly under the treatment of HCQ@ZnS@exo@iRGD. Much better anti-tumor effects were observed when U87 cells were treated with HCQ@ZnS@exo@iRGD under light illumination. (Fig.8a) To visualize apoptotic events, cells were treated with different formulations and stained for apoptosis (cleaved Caspase 3 (cCASP3)) markers. After treatments, the percentage of cCASP3-positive U87 cells treated with HCQ@ZnS@exo@iRGD under light illumination significantly increased with respect to the HCQ@ZnS@exo or non-illuminated HCQ@ZnS@exo@iRGD groups. In contrast, the apoptotic index of U87 cells in free HCQ and HCQ@ZnS were nearly not affected by the treatments. (Fig.8b)

We performed the sphere formation assay to investigate the effect of different formulations on the U87 self-renewal capacity. (Fig. 8c) We found that the average number of colonies formed under suspension cell culture conditions by HCQ@ZnS@exo and HCQ@ZnS@exo@iRGD treated cells was significantly lower than the number formed by free HCQ and HCQ@ZnS, and the sizes of the colonies were also reduced. Notably, using light irradiation will further enhance HCQ@ZnS@exo@iRGD's effect in breaking up the spheroid. Using a Boyden transwell chamber assay, we found that treating U87 cells with HCQ@ZnS@exo@iRGD under light illumination significantly reduced the percentage of invasive cells (Figure S4a). Such treatment also reduced the ability of cells in a monolayer to fill the gap created by pipet scratching in a wound healing assay. (Figure S4b)

These data show that U87 cell viability, stemness and invasiveness, migratory activity were significantly suppressed after HCQ@ZnS@exo@iRGD treatment under light irradiation.

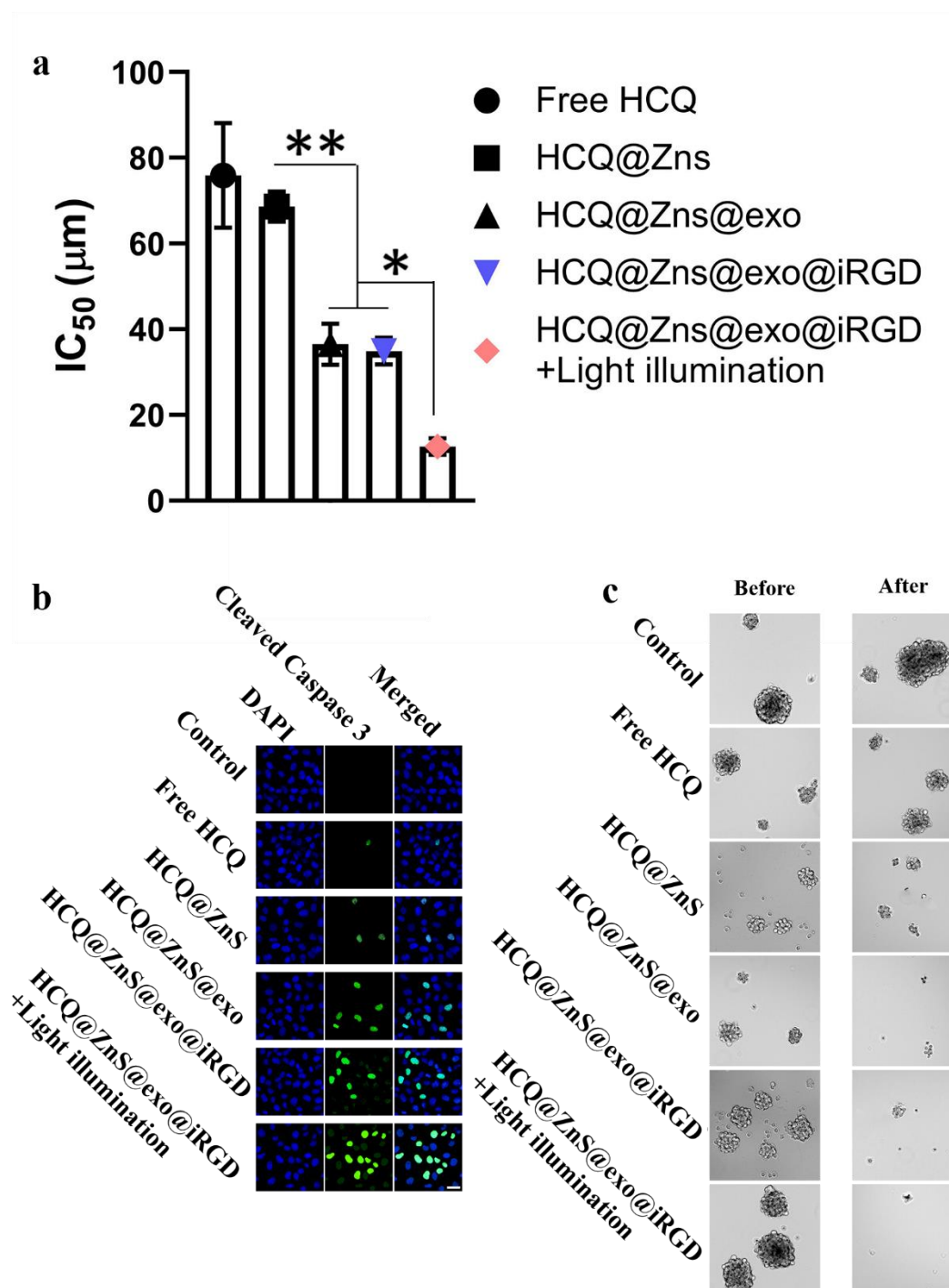


**Figure 8.** Cell viabilities, apoptosis and stemness of U87 cells after treatment with different formulations *in vitro*. **(a)** The IC<sub>50</sub>s for different formulations under different circumstance. Inhibiting autophagy reduces the viability of U87 cells. **(b)** Representative cleaved caspase 3 (green) immunofluorescence of U87 cells after treated with different formulations with/without light illumination. Scale bar is 20 μm. **(c)** suspension culture conditions was used to assess the self-renewal capacity of U87 cells treated with different HCQ formulations. The sphere number and cell number per sphere were counted after 7 days. Scale bar = 100 μm. All results are presented as data from three independent experiments. The data in panels are plotted as the mean ± SD

with the indicated significance (\* $P < 0.05$ , \*\* $P < 0.01$ , according to a Student's t-test).

### 3.10. Biodistribution of nanoparticles *in vivo*

The orthotopic glioblastoma xenograft model was established for the assessments of the targeting ability of Cy 5.5@ZnS@exo@iRGD *in vivo* via IVIS Spectrum imaging system. The results show that the Cy 5.5@ZnS@exo@iRGD displayed a more selective accumulation at the glioblastoma sites 24 h post of injection, compared with the unmodified Cy 5.5@ZnS@exo, Cy 5.5@ZnS and free Cy 5.5 (Fig. 9a). After 24 h, the mice were sacrificed, major organs were excised for *ex vivo* imaging to display the tissue distribution (Fig. 9b). Moreover, the glioblastoma-bearing brains were also excised for *ex vivo* imaging, and the quantitative average radiant efficiency of glioblastoma-bearing brains also confirmed the highest glioblastoma aggregation of Cy 5.5@ZnS@exo@iRGD than the unmodified Cy 5.5@ZnS@exo, Cy 5.5@ZnS and free Cy 5.5 (Fig. 9b). All results indicated Cy 5.5@ZnS@exo@iRGD held the highest glioblastoma targeting effect among different treatments, implying that the iRGD of Cy 5.5@ZnS@exo could easily pass through the BBB and then uptake by the glioblastoma cells. Furthermore, tumor microenvironment of high  $H^+$  and GSH level, pH and redox labile linkers of iRGD will be cleaved and exosome membrane will expose. Due to the homing ability of exosome which extracted from U87 spheroid, Cy 5.5@ZnS@exo may have high affinity with GSC after passing BBB *in vivo*. As expected, the result (Fig. 9b) shows that Cy 5.5@ZnS@exo@iRGD accumulated much more in the brain than other treatment groups.

### 3.11. Anti-glioblastoma efficacy of nanoparticles in glioblastoma bearing mice

The anti-glioblastoma efficacy of nanoparticles was evaluated in the orthotopic glioblastoma (Luc-U87) mice model. The size of the glioblastoma in the brain were measured via the IVIS imaging system by intraperitoneal injection of D-luciferin potassium salt (150 mg/kg). As shown in Fig. 9d, the HCQ@ZnS@exo@iRGD with light irradiation displayed obvious weaker luminescence intensity than other groups, which is consistent with a smallest area of luminescence. The results indicated that HCQ@ZnS@exo@iRGD with light irradiation treatment held a better anti-glioblastoma efficacy than other groups. The glioblastoma grew curved was illustrated in Fig. 9e showing much steeper curves for free HCQ and HCQ@ZnS treatment groups, while treating with HCQ@ZnS@exo@iRGD under light illumination has best efficacy in eliminating GBM among these treatment groups.

The therapeutic efficacy of clinical malignant tumor patients was mainly evaluated by overall survival time and life quality. The survival rate also confirmed the improved efficacy of glioblastoma treatment by applying HCQ@ZnS@exo@iRGD with light irradiation. As shown in Fig. 9f, the survival time showed that the mice treated with HCQ@ZnS@exo@iRGD with light irradiation displayed the longest median survival time (69 days), while PBS, free HCQ, HCQ@ZnS, HCQ@ZnS@exo or HCQ@ZnS@exo@iRGD without light irradiation achieved the median survival times of 29, 31, 31 and 38 days, respectively.

The apoptosis at the glioblastoma sites after various treatments were measured by the annexin V and PI staining. As shown in Fig. 9g, the apoptosis results showed that HCQ@ZnS@exo@iRGD with light irradiation group induced more cell apoptosis than

other groups. CD90 is a multi-structural and multi-functional cell surface receptor involved in cell proliferation, cell differentiation, cell migration and angiogenesis, while CD133 is believed to be associated with tumorigenicity and progression of glioblastoma. Both CD90 and CD133 are often used as surface markers of glioblastoma. Therefore, we checked the expression of CD90 and CD133 in cancer cells in tumors after treatment with different formulations *in vivo*. As shown in Fig.9h, significant reduced expression of CD90 and CD133 following treatment with HCQ@ZnS@exo@iRGD under light illumination was observed, suggesting that HCQ@ZnS@exo@iRGD was effective for targeting and destroying CD90<sup>+</sup>CD133<sup>+</sup> glioblastoma in multiple ways. All these results displayed that HCQ@ZnS@exo@iRGD may efficiently deliver HCQ@ZnS to glioblastoma site for targeting and eliminating GSCs with light irradiation *in vivo*.

No obvious signs of side effects were observed after treatment with HCQ@ZnS@exo@iRGD. No deaths or significant loss of body weight occurred following treatment with HCQ@ZnS@exo@iRGD (Figure S5a). Hematological indices after treatment with HCQ@ZnS@exo@iRGD were similar to those of healthy animals (Figure S5b). These results suggest that the HCQ@ZnS@exo@iRGD shows minimal systemic toxicity *in vivo*.

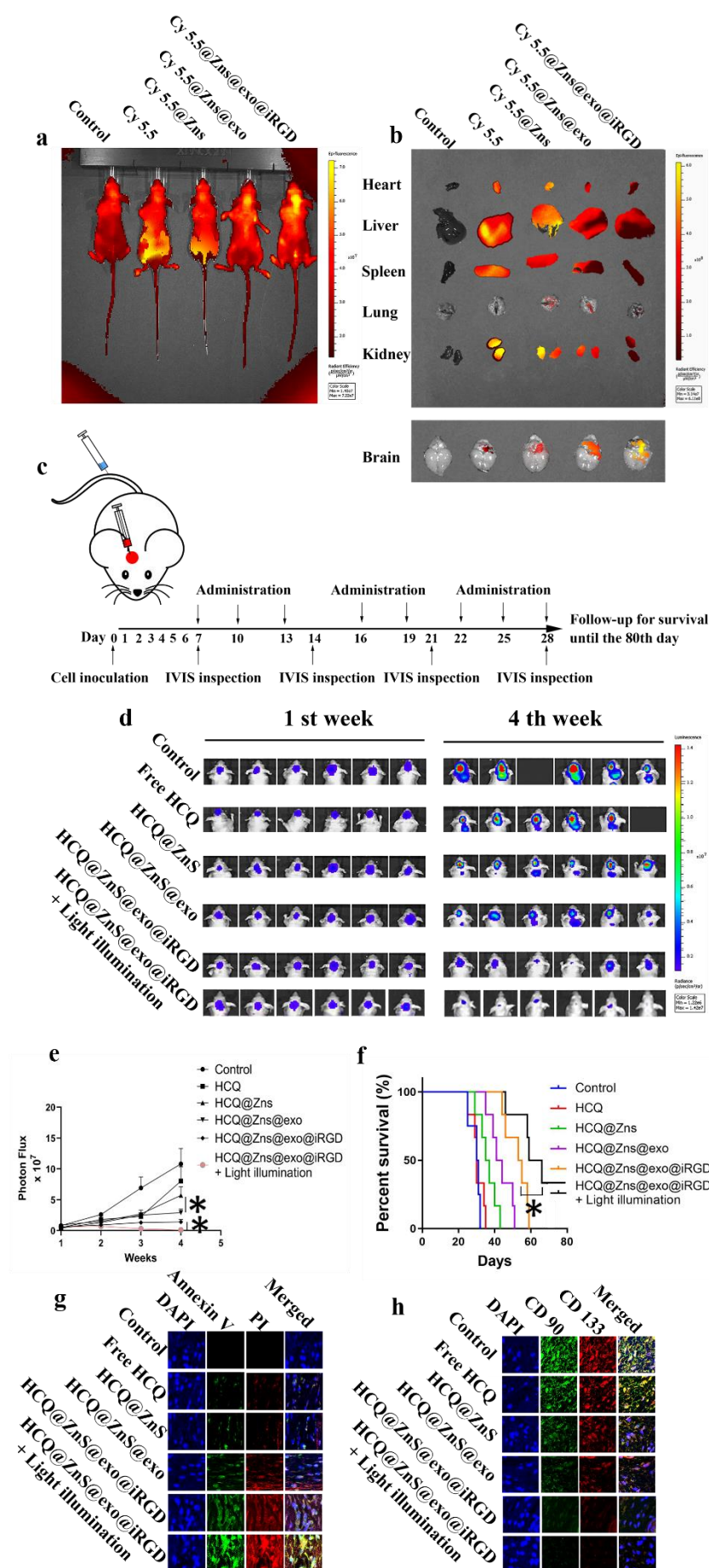




**Figure 9.** *In vivo* distribution and anti-glioblastoma efficacy of Cy 5.5- or HCQ- loaded ZnS nanoparticles on the U87 orthotopic glioblastoma bearing mice model. **(a)** Whole body fluorescence imaging of U87 orthotopic glioblastoma mice at 24 h after tail vein injection of Cy 5.5-loaded ZnS nanoparticles. **(b)** *Ex vivo* fluorescence imaging of the major organs and brain from orthotopic glioblastoma mice. **(c)** Schematic diagram of luciferase expressing orthotopic glioblastoma model and drug treatment. After glioblastoma cell implantation, tumor growth was monitored by IVIS imaging system. **(d)** Real-time bioluminescence images of the orthotopic glioblastoma model nude mice treated with PBS, free HCQ, HCQ@ZnS, HCQ@ZnS@exo or HCQ@ZnS@exo@iRGD with or without light irradiation on day of 7 and 28. The absence of mice in the imaging indicated the death of the mice. **(e)** Quantification of signals from the orthotopic glioblastoma bearing mice ( $n = 6$ ,  $*p < 0.05$ ) on the day of 7, 14, 21 and 28. **(f)** Kaplan-Meier survival curves of the orthotopic glioblastoma nude mice ( $n = 6$ ,  $*p < 0.05$ ). **(g)** Staining of early apoptosis (annexin V) and late apoptosis (propidium iodide, PI) in tumors collected on day 14. **(h)** Immunohistochemical staining of CD90 and CD133 in tumors from mice after different treatments. HCQ@ZnS@exo@iRGD under light illumination significantly reduced expression of both markers. Magnification, 300 $\times$ . ( $n=3$ )

#### 4. Discussion

Photodynamic therapy has shown promising effect in cancer treatment.[36] Metal materials including ZnS, Au and Pt are excellent therapeutic materials, phototherapies achieve a higher selectivity than the conventional treatments towards the tumor sites since only the photosensitizer accumulated in the tumor sites could be activated by the light irradiation.[37] In this study, the HCQ loaded ZnS nanoparticles were synthesized for the combination of chemotherapy and photodynamic therapy. All results confirmed a higher antitumor efficacy of HCQ@ZnS with visible light irradiation than the other groups both *in vitro* and *in vivo*.

HCQ are used to block the late stages of autophagy in *in vitro* studies. Here, we compared the effects of HCQ formulations on cellular morphology, autophagy progression and endo-lysosomal trafficking. We observed major differences in the acidity and morphological appearance of lysosome and autophagosome in cells exposed to HCQ formulations. While HCQ@ZnS@exo and HCQ@ZnS@exo@iRGD treated cells displayed clear phenotypes associated with an inhibition of the degradation capacity of lysosomes such as the presence of intact cytoplasm in the lysosomal lumen and a loss of acidity, HCQ and HCQ@ZnS treated cells did not present a similar profile. In line with these observations, we find a decrease in LysoTracker Red-positive puncta upon HCQ@ZnS@exo and HCQ@ZnS@exo@iRGD.

Similar with numerous early studies accumulations of autophagic vesicles in HCQ treated cells have already been observed in our experiment.[38] It has remained unclear whether this phenomenon was due to an inhibition of fusion or a block in lysosomal degradation. Our detailed examination on the step of autophagy that is inhibited by HCQ@ZnS@exo and HCQ@ZnS@exo@iRGD revealed that this compound blocks



autophagosome-lysosome fusion and not degradation capacity of lysosomes as previously assumed. Free HCQ and HCQ@ZnS in contrast, inhibits the degradation capacity of lysosomes by decreasing their acidity, but it can also impair fusion between autophagosomes and lysosomes. Our observations confirm that HCQ impairs autophagosome fusion with lysosomes.

By neutralizing lysosomes, HCQ inhibits autophagy and therefore shows potential as an anticancer drug. However, its clinical usefulness is severely limited because highly effective doses are required to compensate for its nonselective distribution *in vivo* and its inefficiency to cross BBB and target GSCs and release its cargo in the TME.[39] Here we tried to avert all 3 problems by encapsulating HCQ in hollow ZnS nanoparticles coated with hybrid exosome. We show using *in vitro* and *in vivo* approaches that HCQ@ZnS@exo@iRGD specifically targets U87 tumors and efficiently accumulates HCQ within GSCs and lysosomes. This accumulation inhibits autophagy, which enhances the antitumor efficiency of ROS and H<sub>2</sub>S.

Surface morphology, particle size and  $\zeta$ -potential are important characteristics of drug loaded nanocarriers.[40] They have been demonstrated to play important roles in determining cellular and tissue uptake efficiency and toxic effect on cells.[41] Smooth surface morphology could prove the uniformity and stability of the system.[42] An obvious core-shell structured morphology can be observed in Fig. 4b, suggesting that exosome membrane and iRGD-derived liposome may modify onto the surface of HCQ@ZnS and showing an outer layer on the vector. The size and zeta potential of NPs not only determine their colloidal stability but also influence the effectiveness of their interaction with negatively charged cell membranes, which is the pivotal step for successful cellular uptake. Unmodified HCQ@ZnS had a slight positive surface charge, due to the existence of cationic Zn<sup>2+</sup>.  $\zeta$ -potential of HCQ@ZnS@exo and HCQ@ZnS@exo@iRGD decreased significantly, indicating that anionic exosome membrane and/or iRGD-derived liposome located on the surface of HCQ@ZnS neutralized the charge of the nanoparticles. The positive surface charge is necessary to ensure the uptake of complexes by cells due to electrostatic interactions between negatively charged cellular membranes and positively charged nanocarriers.

The fastest release of HCQ from HCQ@ZnS@exo@iRGD at pH 5.5 with high GSH could prove that the iRGD-PEG-ss-aPS with a pH- and GSH-sensitive linker have effect on the characteristic of the HCQ@ZnS@exo@iRGD. At acidic condition with high level of GSH, the aconitic anhydride bond and cystamine linker would rupture and change the structure of the HCQ@ZnS@exo@iRGD, and let the HCQ release more freely from the carriers to perform treating effect.

Selective, efficient internalization of HCQ@ZnS@exo@iRGD and the resulting accumulation of HCQ in lysosomes means not only greater therapeutic effect but also lower toxicity. Encapsulating HCQ in HCQ@ZnS@exo@iRGD significantly reduced its distribution to the small intestine, where HCQ elicits gastrointestinal adverse effects; encapsulation also attenuated the ability of HCQ to induce myelosuppression.

In the present study, the release of HCQ from the ZnS nanoparticles partly depended

on the levels of  $H^+$  and GSH. Our results verified that the HCQ@ZnS@exo@iRGD held completely different drug release behavior in different pH with/out GSH, revealing that the ZnS nanoparticles having excellent pH and GSH stimuli response to realize the controlled release behavior of HCQ. The responsive drug release behavior could effectively reduce the side effect to normal cells, as the pH and GSH level are much higher in TME compared to normal environment. The cellular uptake of HCQ@ZnS@exo@iRGD by MCF10A cells verified that the HCQ@ZnS@exo@iRGD effectively reduced the toxicity of HCQ to normal cell. The *in vivo* distribution results also confirmed that HCQ@ZnS@exo@iRGD had effectively reduced the possible toxicity of HCQ@ZnS@exo@iRGD in normal organs. All above results suggested that the combination therapy enhanced the anti-GBM efficacy with reduced side effect in GBM treatment.

In various experiments, we compared HCQ@ZnS, HCQ@ZnS@exo and HCQ@ZnS@exo@iRGD, allowing us to isolate the effects of HCQ encapsulation and the effects of the hybrid exosome. Our results suggest that encapsulating HCQ in HCQ@ZnS@exo and HCQ@ZnS@exo@iRGD allows the nanocarrier to evade capture by the RES and to target tumors passively via the EPR effect; free HCQ, in contrast, distributes nonselectively throughout the body. The HCQ@ZnS@exo@iRGD contains an iRGD peptide that targets ITGAV-ITGB3/integrin  $\alpha_v\beta_3$  receptors overexpressed on tumor cells, as well as a pH- and GSH-sensing iRGD that becomes cleaved in TME. Then the exposed exosome membrane layer could specifically guide the HCQ loaded nanoparticles to GSCs. Both these functionalities allow HCQ@ZnS@exo@iRGD to be efficiently internalized by GSCs.

The transportation of antitumor agents to cross the BBB remains the main obstacles for effective GBM treatment.[43] In previous studies, iRGD conjugation were proved to be an efficient strategy for drug delivery from nanoparticles. In this study, we synthesized hybrid exosome comprising a dual responsive iRGD-derived phosphatidylserine and exosome excreted by human U87 glioblastoma spheroids for the BBB crossing and GSCs targeting. Meanwhile, the encapsulation of HCQ into the hollow ZnS nanoparticles can effectively combine chemotherapy with photodynamic therapy. Additionally, the obtained HCQ@ZnS@exo@iRGD displayed good stability with controlled drug release behavior, which showing great promise for the treatment of brain tumor.

Owing to the modification of iRGD ligand with pH- and redox-cleavable linker on the surface of HCQ@ZnS@exo, the *in vivo* cellular uptake of HCQ@ZnS@exo@iRGD in the orthotopic glioblastoma mice model was much higher than those of ZnS nanoparticles without iRGD ligand modification, revealing that the iRGD modified ZnS nanoparticles could effectively pass through the BBB and then target the GSCs. The results were also consistent with the biodistribution of HCQ@ZnS@exo@iRGD *in vivo*. Since the protein expressions of integrin  $\alpha_v\beta_3$  and neuropilin-1 are relatively high in the endothelial cells and GBM cell, hybrid exosome makes HCQ@ZnS much easier for the BBB crossing and tumor penetration in the GBM sites. Therefore, the hybrid exosome-modified ZnS nanoparticles are promising alternative for therapeutic

delivery to the GSCs.

These findings indicate that this “smart” dual responsive, multi-functional delivery system may expand and accelerate clinical application of HCQ chemotherapy. HCQ@ZnS@exo@iRGD is a leading drug formulation of HCQ with great potential to be optimized further for potency as an autophagy inhibitor, and hollow ZnS nanoparticles covered with hybrid exosome, as a drug delivery carrier, may also be used to deliver other autophagy modulators. For *in vivo* special autophagy modulation applications in which the modulators just need to reach the diseased organs or tissue and enter into the cells, the hybrid exosome would be perfect to improve the modulator delivery and reduce the toxicity derived from nonspecific interactions of drugs with cells. On the other hand, for applications in extensively conducted combination therapy around “autophagy inhibition +X,” HCQ@ZnS@exo@iRGD may be ideally employed.

Glioblastoma is a devastating and deadly malignant primary brain tumor in adults. It nearly always relapses after initial conventional treatment, and frequently exhibits resistance to current therapeutics.[44] The reason that may explain the recurrence and treatment resistance is the presence of GBM stem cells (GSCs). The approaches of target eliminating GSCs might be effective for GBM eradication.[45] However, the strategies of identifying or targeting GSCs have been proved to be unsuccessful recently. Exosomes are 30–100 nm extracellular vehicles (EVs) released by all living cells, including GBM cells and GSCs.[46] These small vesicles contain lots of bioactive materials in the form of proteins, DNA, mRNA, miRNA and lipids, acting as information carriers, and playing important roles in intercellular communication by transferring their molecular contents to recipient cells. Exosomes derived from GSCs carried membrane receptors and signaling proteins that participate in glioblastoma progression and purposely aim for GSCs.[47]

In the present experimental study, exosomes were isolated from human U87 glioblastoma spheroids cell culture media and characterized. It is indicated that GSC exosome exposure increased the stemness and tumorigenicity of non-GSC GBM cells. Therefore, utilizing special GSCs related exosome would discover new targets for GBM therapeutics.

The current clinical studies are aiming to determine whether autophagy inhibition has a beneficial role in tumor treatments. Because HCQ are the FDA-approved drugs inhibiting autophagy, these compounds have extensively been used to test whether the block of this pathway improves tumor treatments. Our study underlines that HCQ loaded into hybrid exosome covered ZnS nanoparticles are indisputably substantially impairing the autophagic flux. Therefore, positive effects on tumor regression in the orthotopic glioblastoma mice model by treatment with HCQ@ZnS@exo@iRGD has been observed in our research.

## 5. Conclusion

In summary, we designed a new multifunctional nanoplatfrom based on multi-shelled hollow spheres for PDT/chemotherapeutic synergistic cancer treatment. The developed HCQ@ZnS@exo@iRGD possessed the following features: (1) GSCs targeting, (2) efficient ROS/H<sub>2</sub>S generation in lysosome under light irradiation, (3) blocking autophagy flux by HCQ, which enabled simultaneous H<sub>2</sub>S therapy, chemotherapy, and phototherapy. A good understanding of the *in vivo* behavior of the as-obtained HCQ@ZnS@exo@iRGD, such as their quantitative pharmacokinetics, biodistribution, and long-term toxicity, is of importance and requires further exploration. HCQ@ZnS@exo@iRGD opens a new therapeutic window for the treatment of GBM. HCQ@ZnS@exo@iRGD and stands out as a cost-effective therapy reagent in the field of nanomedicine.

### **Conflicts of interest**

The authors have no existing conflicts to declare.

### **Acknowledgements**

This project was supported by the National Natural Science Foundation of China (81860629) and the Natural Science Foundation of Guangxi Province, (2019GXNSFAA245095). The authors thank the Mark Wainwright Analytical Centre at the University of New South Wales.

## References:

- [1] A.M. Molinaro, J.W. Taylor, J.K. Wiencke, M.R. Wrensch, Genetic and molecular epidemiology of adult diffuse glioma, *Nature Reviews Neurology* 15(7) (2019) 405-417.
- [2] A. Dirkse, A. Golebiewska, T. Buder, P.V. Nazarov, A. Muller, S. Poovathingal, N.H.C. Brons, S. Leite, N. Sauvageot, D. Sarkisjan, M. Seyfrid, S. Fritah, D. Stieber, A. Michelucci, F. Hertel, C. Herold-Mende, F. Azuaje, A. Skupin, R. Bjerkvig, A. Deutsch, A. Voss-Böhme, S.P. Niclou, Stem cell-associated heterogeneity in Glioblastoma results from intrinsic tumor plasticity shaped by the microenvironment, *Nature Communications* 10(1) (2019) 1787.
- [3] Mario L. Suvà, E. Rheinbay, Shawn M. Gillespie, Anoop P. Patel, H. Wakimoto, Samuel D. Rabkin, N. Riggi, Andrew S. Chi, Daniel P. Cahill, Brian V. Nahed, William T. Curry, Robert L. Martuza, Miguel N. Rivera, N. Rossetti, S. Kasif, S. Beik, S. Kadri, I. Tirosh, I. Wortman, A.K. Shalek, O. Rozenblatt-Rosen, A. Regev, David N. Louis, Bradley E. Bernstein, Reconstructing and Reprogramming the Tumor-Propagating Potential of Glioblastoma Stem-like Cells, *Cell* 157(3) (2014) 580-594.
- [4] W. Lv, Z. Zhang, K.Y. Zhang, H. Yang, S. Liu, A. Xu, S. Guo, Q. Zhao, W. Huang, A Mitochondria-Targeted Photosensitizer Showing Improved Photodynamic Therapy Effects Under Hypoxia, 55(34) (2016) 9947-9951.
- [5] W. Yu, Y. Wang, J. Zhu, L. Jin, B. Liu, K. Xia, J. Wang, J. Gao, C. Liang, H. Tao, Autophagy inhibitor enhance ZnPc/BSA nanoparticle induced photodynamic therapy by suppressing PD-L1 expression in osteosarcoma immunotherapy, *Biomaterials* 192 (2019) 128-139.
- [6] Y. Wang, K. Shi, L. Zhang, G. Hu, J. Wan, J. Tang, S. Yin, J. Duan, M. Qin, N. Wang, D. Xie, X. Gao, H. Gao, Z. Zhang, Q. He, Significantly enhanced tumor cellular and lysosomal hydroxychloroquine delivery by smart liposomes for optimal autophagy inhibition and improved antitumor efficiency with liposomal doxorubicin, *Autophagy* 12(6) (2016) 949-962.
- [7] A. Ruiz, S. Rockfield, N. Taran, E. Haller, R.W. Engelman, I. Flores, P. Panina-Bordignon, M. Nanjundan, Effect of hydroxychloroquine and characterization of autophagy in a mouse model of endometriosis, *Cell Death & Disease* 7(1) (2016) e2059-e2059.
- [8] Y. Yang, W. Zhu, L. Cheng, R. Cai, X. Yi, J. He, X. Pan, L. Yang, K. Yang, Z. Liu, W. Tan, M. Chen, Tumor microenvironment (TME)-activatable circular aptamer-PEG as an effective hierarchical-targeting molecular medicine for photodynamic therapy, *Biomaterials* 246 (2020) 119971.
- [9] S. Ruan, R. Xie, L. Qin, M. Yu, W. Xiao, C. Hu, W. Yu, Z. Qian, L. Ouyang, Q. He, H. Gao, Aggregable Nanoparticles-Enabled Chemotherapy and Autophagy Inhibition Combined with Anti-PD-L1 Antibody for Improved Glioma Treatment, *Nano Letters* 19(11) (2019) 8318-8332.
- [10] M.S.M. Saifullah, M. Asbahi, M. Binti-Kamran Kiyani, S. Tripathy, E.A.H. Ong, A. Ibn Saifullah, H.R. Tan, T. Dutta, R. Ganesan, S. Valiyaveetil, K.S.L. Chong, Direct Patterning of Zinc Sulfide on a Sub-10 Nanometer Scale via Electron Beam Lithography, *ACS Nano* 11(10) (2017) 9920-9929.
- [11] C. Fang, D. Cen, Y. Wang, Y. Wu, X. Cai, X. Li, G. Han, ZnS@ZIF-8 core-shell nanoparticles incorporated with ICG and TPZ to enable H<sub>2</sub>S-amplified synergistic therapy, *Theranostics* 10(17) (2020) 7671-7682.
- [12] Y. Cheng, Y. Chang, Y. Feng, H. Jian, X. Wu, R. Zheng, K. Xu, H. Zhang, Bismuth Sulfide Nanorods with Retractable Zinc Protoporphyrin Molecules for Suppressing Innate Antioxidant Defense System and Strengthening Phototherapeutic Effects, 31(10) (2019) 1806808.
- [13] S. Yu, Z. Xie, M. Ran, F. Wu, Y. Zhong, M. Dan, Y. Zhou, Zinc ions modified InP quantum dots for enhanced photocatalytic hydrogen evolution from hydrogen sulfide, *Journal of Colloid and*



Interface Science 573 (2020) 71–77.

[14] C. Yan, D. Liu, L. An, Y. Wang, Q. Tian, J. Lin, S. Yang, Magnetic–Photoacoustic Dual-Mode Probe for the Visualization of H<sub>2</sub>S in Colorectal Cancer, *Analytical Chemistry* 92(12) (2020) 8254–8261.

[15] A. Raposo Moreira Dias, L. Boderio, A. Martins, D. Arosio, S. Gazzola, L. Belvisi, L. Pignataro, C. Steinkühler, A. DalCorso, C. Gennari, U. Piarulli, Synthesis and Biological Evaluation of RGD and isoDGR–Monomethyl Auristatin Conjugates Targeting Integrin  $\alpha$ V $\beta$ 3, 14(9) (2019) 938–942.

[16] X. Xia, X. Yang, P. Huang, D. Yan, ROS-Responsive Nanoparticles Formed from RGD–Epothilone B Conjugate for Targeted Cancer Therapy, *ACS Applied Materials & Interfaces* 12(16) (2020) 18301–18308.

[17] R. Kalluri, V.S. LeBleu, The biology and function and biomedical applications of exosomes, 367(6478) (2020) eaau6977.

[18] R. Munagala, F. Aqil, J. Jeyabalan, R.C. Gupta, Bovine milk-derived exosomes for drug delivery, *Cancer Letters* 371(1) (2016) 48–61.

[19] D.G. Phinney, M.F. Pittenger, Concise Review: MSC-Derived Exosomes for Cell-Free Therapy, 35(4) (2017) 851–858.

[20] B. Illes, P. Hirschle, S. Barnert, V. Cauda, S. Wuttke, H. Engelke, Exosome-Coated Metal–Organic Framework Nanoparticles: An Efficient Drug Delivery Platform, *Chemistry of Materials* 29(19) (2017) 8042–8046.

[21] J. Mo, L. Wang, X. Huang, B. Lu, C. Zou, L. Wei, J. Chu, P.K. Eggers, S. Chen, C.L. Raston, J. Wu, L.Y. Lim, W. Zhao, Multifunctional nanoparticles for co-delivery of paclitaxel and carboplatin against ovarian cancer by inactivating the JMJD3-HER2 axis, *Nanoscale* 9(35) (2017) 13142–13152.

[22] M. Tayebi, Y. Zhou, P. Tripathi, R. Chandramohanadas, Y. Ai, Exosome Purification and Analysis Using a Facile Microfluidic Hydrodynamic Trapping Device, *Analytical Chemistry* (2020).

[23] Q. Yan, A.P. Wu, H.J. Yan, Y.Y. Dong, C.G. Tian, B.J. Jiang, H.G. Fu, Gelatin-assisted synthesis of ZnS hollow nanospheres: the microstructure tuning, formation mechanism and application for Pt-free photocatalytic hydrogen production, *Crystengcomm* 19(3) (2017) 461–468.

[24] S. Kannan, N.P. Subiramaniam, M. Sathishkumar, Investigation on the structural, optical and photocatalytic degradation properties of ZnS/Mn:ZnS thin films under visible light irradiation, *Materials Today: Proceedings* (2020).

[25] G.K. Patel, M.A. Khan, H. Zubair, S.K. Srivastava, M.d. Khushman, S. Singh, A.P. Singh, Comparative analysis of exosome isolation methods using culture supernatant for optimum yield, purity and downstream applications, *Scientific Reports* 9(1) (2019) 5335.

[26] R.H. Fang, Y. Jiang, J.C. Fang, L. Zhang, Cell membrane-derived nanomaterials for biomedical applications, *Biomaterials* 128 (2017) 69–83.

[27] L. Vera-Ramirez, S.K. Vodnala, R. Nini, K.W. Hunter, J.E. Green, Autophagy promotes the survival of dormant breast cancer cells and metastatic tumour recurrence, *Nature Communications* 9(1) (2018) 1944.

[28] J. Xu, H. Sun, G. Huang, G. Liu, Z. Li, H. Yang, L. Jin, X. Cui, L. Shi, T. Ma, A. Kameyama, W. Dong, A fixation method for the optimisation of western blotting, *Scientific Reports* 9(1) (2019) 6649.

[29] E. Kinoshita, E. Kinoshita-Kikuta, K. Karata, T. Kawano, A. Nishiyama, M. Yamato, T. Koike, Specific glutamic acid residues in targeted proteins induce exaggerated retardations in Phos-tag SDS-PAGE migration, 38(8) (2017) 1139–1146.

- [30] Y. Li, J. Li, Y.M. Woo, Z. Shen, H. Yao, Y. Cai, M.C.-m. Lin, W.S. Poon, Enhanced expression of Vastatin inhibits angiogenesis and prolongs survival in murine orthotopic glioblastoma model, *BMC Cancer* 17(1) (2017) 126.
- [31] L. Kong, X.H. Tian, H. Wang, Y.H. Gao, Q. Zhang, J.X. Yang, H.P. Zhou, S.Y. Zhang, Y.P. Tian, Coordination coupling enhanced two-photon absorption of a ZnS-based microhybrid for two-photon microscopy imaging in HepG2, *Nanoscale* 9(23) (2017) 7901-7910.
- [32] C. Du, Y. Liang, Q. Ma, Q. Sun, J. Qi, J. Cao, S. Han, M. Liang, B. Song, Y. Sun, Intracellular tracking of drug release from pH-sensitive polymeric nanoparticles via FRET for synergistic chemo-photodynamic therapy, *Journal of Nanobiotechnology* 17(1) (2019) 113.
- [33] K. Boriachek, M.N. Islam, A. Möller, C. Salomon, N.-T. Nguyen, M.S.A. Hossain, Y. Yamauchi, M.J.A. Shiddiky, Biological Functions and Current Advances in Isolation and Detection Strategies for Exosome Nanovesicles, 14(6) (2018) 1702153.
- [34] K. Kalishwaralal, W.Y. Kwon, K.S. Park, Exosomes for Non-Invasive Cancer Monitoring, 14(1) (2019) 1800430.
- [35] W. Chen, L. Li, X. Zhang, Y. Liang, Z. Pu, L. Wang, J. Mo, Curcumin: a calixarene derivative micelle potentiates anti-breast cancer stem cells effects in xenografted, triple-negative breast cancer mouse models, *Drug delivery* 24(1) (2017) 1470-1481.
- [36] J. Mo, M. Li, X. Chen, Q. Li, Calixarene-mediated assembly of water-soluble C60-attached ultrathin graphite hybrids for efficient activation of reactive oxygen species to treat neuroblastoma cells, *Chem Commun (Camb)* 56(53) (2020) 7325-7328.
- [37] W. Zhu, Y. Yang, Q. Jin, Y. Chao, L. Tian, J. Liu, Z. Dong, Z. Liu, Two-dimensional metal-organic-framework as a unique theranostic nano-platform for nuclear imaging and chemo-photodynamic cancer therapy, *Nano Research* 12(6) (2019) 1307-1312.
- [38] K. Wang, Y. Wei, W. Liu, L. Liu, Z. Guo, C. Fan, L. Wang, J. Hu, B. Li, Mechanical Stress-Dependent Autophagy Component Release via Extracellular Nanovesicles in Tumor Cells, *ACS Nano* 13(4) (2019) 4589-4602.
- [39] M. Condello, G. Mancini, S. Meschini, The Exploitation of Liposomes in the Inhibition of Autophagy to Defeat Drug Resistance, *Front Pharmacol* 11 (2020) 787-787.
- [40] G. Spezzati, K. Fant, A. Ahniyaz, M. Lundin-Johnson, E.J.M. Hensen, H. Langermans, J.P. Hofmann, Synthesis, Physicochemical Characterization, and Cytotoxicity Assessment of CeO<sub>2</sub> Nanoparticles with Different Morphologies, 2017(25) (2017) 3184-3190.
- [41] K. Kedra-Królik, K.M. Rosso, P. Zarzycki, Probing size-dependent electrokinetics of hematite aggregates, *Journal of Colloid and Interface Science* 488 (2017) 218-224.
- [42] M.M. Allard, S.N. Merlos, B.N. Springer, J. Cooper, G. Zhang, D.S. Boskovic, S.R. Kwon, K.E. Nick, C.C. Perry, Role of TiO<sub>2</sub> Anatase Surface Morphology on Organophosphorus Interfacial Chemistry, *The Journal of Physical Chemistry C* 122(51) (2018) 29237-29248.
- [43] L. Wen, Y. Tan, S. Dai, Y. Zhu, T. Meng, X. Yang, Y. Liu, X. Liu, H. Yuan, F. Hu, VEGF-mediated tight junctions pathological fenestration enhances doxorubicin-loaded glycolipid-like nanoparticles traversing BBB for glioblastoma-targeting therapy, *Drug delivery* 24(1) (2017) 1843-1855.
- [44] J.M. Przystal, N. Hajji, C. Khozoie, A. Renziehausen, Q. Zeng, F. Abaitua, A. Hajitou, K. Suwan, E. Want, J. Bomalaski, P. Szlosarek, K. O'Neill, T. Crook, N. Syed, Efficacy of arginine depletion by ADI-PEG20 in an intracranial model of GBM, *Cell Death & Disease* 9(12) (2018) 1192.
- [45] M. Lunski, J. Smyth, J. Vaughn, Z. Sheng, R. Gourdie, B. Purow, S. Lamouille, Abstract 4284:

Targeting notch signaling in glioblastoma cancer stem cells through modulation of Connexin43 function, *Cancer Research* 79(13 Supplement) (2019) 4284.

[46] K. Gabrusiewicz, X. Li, J. Wei, Y. Hashimoto, A.L. Marisetty, M. Ott, F. Wang, D. Hawke, J. Yu, L.M. Healy, A. Hossain, J.C. Akers, S.N. Maiti, S. Yamashita, Y. Shimizu, K. Dunner, M.A. Zal, J.K. Burks, J. Gumin, F. Nwajei, A. Rezavanian, S. Zhou, G. Rao, R. Sawaya, G.N. Fuller, J.T. Huse, J.P. Antel, S. Li, L. Cooper, E.P. Sulman, C. Chen, C. Geula, R. Kalluri, T. Zal, A.B. Heimberger, Glioblastoma stem cell-derived exosomes induce M2 macrophages and PD-L1 expression on human monocytes, *Oncolmmunology* 7(4) (2018) e1412909.

[47] M. Veletić, M.T. Barros, I. Balasingham, S. Balasubramaniam, A Molecular Communication Model of Exosome-mediated Brain Drug Delivery, *Proceedings of the Sixth Annual ACM International Conference on Nanoscale Computing and Communication*, Association for Computing Machinery, Dublin, Ireland, 2019, p. Article 22.